IR-80-2059R

MHD MATERIALS - SEED/SLAG INTERACTIONS AND EFFECTS

QUARTERLY PROGRESS REPORT

January - March 1980

Samuel J. Schneider
Project Manager

Center for Materials Science
U. S. Department of Commerce
National Bureau of Standards
Washington, D. C. 20234

PREPARED FOR THE UNITED STATES
DEPARTMENT OF ENERGY
MHD OFFICE

TABLE OF CONTENTS

I. SUMMARY OF PROGRESS TO DATE

1. Thermochemistry of Seed and Slag

Vapor pressure data of K(g) over $KAlSiO_4$ as a function of bulk composition and 1/T are reported. The bulk composition range varies from 28.9 to 10.7 wt% K_2O while the K pressure decreases by 3 orders of magnitude. Some non-equilibrium effects are shown for compositions containing only small amounts of $KAlSiO_4$. Mullite was the only crystalline residue identified at the conclusion of the experiment. Vapor pressure data of SiO(g) and O_2(g) over the $KAlSiO_4$ showed an activity of SiO_2 close to unity. Measurements of the K pressure over $KAlSiO_4$ and calcium silicate salts indicated complete removal of the K_2O at 1945 K.

Additional evidence supporting the existence of ($KAlO_2$-K_2CO_3) ss is presented. Melts with known phase equilibrium properties in the system K_2O-CaO-Al_2O_3-SiO_2 are being prepared for vaporization studies. A quasichemical melt polymerization model for treatment of K_2O-CaO-FeO_x-Al_2O_3-SiO_2 equilibria is discussed.

2. Electrical Conductivity and Polarization

The electrical conductivity of $YCrO_3$ doped with 5% Ca has been measured in a highly reducing atmosphere at temperatures from 1300 to 1600 °C. The samples are not single phase in composition, however, and this may have caused some errors in the bulk conductivity values due to hair-line cracks or phase boundaries.

Several polarization experiments have been completed using slag (Bow, NH) as an electrolyte and using platinum as electrodes. These were made in a specially designed cell incorporating four probes to allow polarization to be measured at any probe as a function of time at a given temperature and for a preset condition regarding charge transfer (constant current or constant voltage).

The electrical conductivity of a Bow, NH slag sample containing an added amount of iron has been measured. At lower temperatures (1200 °C) the conductivity increases nearly proportional to the added iron but at higher temperatures (above 1350 °C) the conductivity increased by a factor of 5 when the iron content was doubled. This increase may be due to the decrease in viscosity associated with iron addition and/or equivalent silica decrease.

3. Corrosion of Downstream Components

Type 316 stainless steel tubes, cooled to 400 °C, 500 °C, and 590 °C, were exposed to oxygen rich hot gas streams seeded with K_2SO_4. Optical, SEM, and EDX analysis indicate the geometric and chemical nature of the deposits and reaction zones to be similar to those of Type 304 stainless steel exposed previously under the same conditions. As in those cases, Fe appears to have penetrated the farthest into the salt deposit region while the dispersion of Ni in the reaction zone area remains the most difficult to follow. The extent of wastage (weight loss) of Type 316 and Type 304 stainless steel exposed at 590 °C and 400 °C to K_2SO_4 seeded oxygen rich hot gas streams was also determined.

In the coming quarter further exposure tests will be conducted on Type 304 and Type 316 stainless steels to determine wastage under oxygen rich conditions with a seed of 80 percent by weight K_2CO_4 and 20 percent by weight K_2SO_4.

II. DETAILED DESCRIPTION OF TECHNICAL PROGRESS

1. Thermochemistry of Seed and Slag (E. R. Plante and L. P. Cook)

A. Vaporization Studies (E. R. Plante)

Progress: Vapor pressure measurements on $KAlSiO_4$ were concluded. Measurements on a selected composition in the K_2O-CaO-Al_2O_3-SiO_2 system were started.

The K_2O-Al_2O_3-SiO_2 system has the potential for forming several stable or metastable phase assemblages in which the K_2O activity is fixed according to the phase rule. These include $KAlSiO_4$, $K_2O{\cdot}9Al_2O_3$, $KAlSi_2O_6$; Al_2O_3, $3Al_2O_3{\cdot}2SiO_2$; and $KAlSi_2O_6$, $KAlSi_3O_8$, $3Al_2O_3{\cdot}2SiO_2$. While analysis of the experimental results obtained is not entirely complete, no evidence that the K pressure was independent of bulk composition of the sample was obtained. This is in agreement with previous studies from this laboratory in which constant potassium pressures were not observed even though $KAlSiO_4$, $K_2O{\cdot}9Al_2O_3$ and $KAlSi_2O_6$ crystalline phases were identified as being present in the sample. This represents non-equilibrium behavior in the measurements. Other evidence for non-equilibrium behavior is shown for the experiment in Figure 1. Here, the observed K pressures are greater when the temperature is decreased even though the bulk K_2O composition decreased in the first part of the experiment. This effect is likely due to depletion of $KAlSiO_4$ from the sample. At the highest temperature (1880 K) partial melting probably caused a redistribution of some remaining $KAlSiO_4$ by either bringing the crystals to the surface or dissolving them in the melt. This effect was noted only in the experiments for which the remaining $KAlSiO_4$ phase was becoming small.

Some representative vapor pressures of K as a function of 1/T and bulk K_2O concentration are given in this report. Figure 2 shows K pressure data as a function of 1/T at various bulk K_2O compositions. The data shown was obtained during experiments in which the sample temperature was decreased throughout the run. Bulk K_2O concentrations were calculated from the integrated ion current data ($I^{+}\Delta t\sqrt{T}$) and represent the K_2O concentration that would exist if the sample were a homogeneous solution. The calculation of bulk composition did not include loss of SiO_2 which became appreciable toward the end of the experiment at higher temperatures. Linearity of the vapor pressure data with 1/T was better for the experiments in which the temperature decreased than for those in which the temperature was increased. This may be due to better mixing of the $KAlSiO_4$ on melting. The data shown represent an extremely wide range of concentration and temperature. The K pressure at constant temperature decreases by over

3 orders of magnitude when the K_2O bulk composition decreases from 29 wt% K_2O to 11 wt% K_2O. At the highest temperature, 2160 K, the sample should be entirely molten and under these conditions slow kinetics due to complex crystal chemistry is not a possibility. The activity of K_2O in the melt is so low that it leads to the question of whether the K_2O concentration could be as high as 11 wt%. Assuming an error of 30% in the mass spectrometer constant, the K_2O concentration might be as low as 3 wt%.

During a considerable portion of the experiment, measurements of the SiO^+ intensity were possible and these data along with measured O_2^+ intensities were used to calculate the product $P_{SiO} \cdot P_{O_2}^{1/2}$ which is related to the activity of SiO_2 and K_p for pure $SiO_2(\ell)$. These data showed that the activity of SiO_2 is close to unity for this system.

The experiment was finally terminated because the P_{SiO} was greater than P_K and it appeared that the sample might become exhausted in SiO_2 before all of the K_2O was evaporated. The sample consisted of a very hard crystalline mass embedded in a glassy matrix. Heating in hot (100°C) dilute HF (~30% conc. HF in H_2O) dissolved the glassy matrix but not the crystalline mass. An x-ray diffraction pattern showed the crystalline material to be mullite ($3Al_2O_3 \cdot 2SiO_2$). It is presumed that in the final stages of the experiment, crystalline mullite was in equilibrium with a liquid phase containing K_2O, SiO_2 and Al_2O_3.

Measurements on a sample containing 49.84 wt% $KAlSiO_4$, 16.47% Ca_2SiO_4, 16.47% $Ca_2Al_2SiO_7$ and 17.21% $Ca_3Si_2O_7$ were begun. The sample contained each of the above phases in an intimately mixed form. The early stage of the evaporation is expected to be described by the reaction

$$2KAlSiO_4(c) + 7Ca_2SiO_4 = 4Ca_3Si_2O_7 + Ca_2Al_2SiO_7 + 2K(g) + O_2(g) \quad (1)$$

Figure 3 shows K pressure data during the early stages of evaporation up to the point where the Ca_2SiO_4 phase should be exhausted. In addition, pressures calculated from the literature at 1400, 1600 and 1800 K are shown for comparison. The agreement between the experimental and calculated pressures are reasonable although the experimental slope is significantly steeper. Additional measurements on this composition were made. It proved possible to vaporize all the K_2O from the sample at 1945 K. This appears to confirm the suspected effect of CaO in ameliorating K_2O capture by Al_2O_3 and SiO_2.

B. Phase Equilibrium Experiments (L. P. Cook)

1. System K_2O-CaO-Al_2O_3-SiO_2

For vaporization studies, a composition consisting of 49.8 wt% $KAlSiO_4$, 16.5 wt% Ca_2SiO_4, 17.2 wt% $Ca_3Si_2O_7$, and 16.5 wt% $Ca_2Al_2SiO_7$ was prepared. It was thought that this would give a large range of possible potassium pressures [1]. Measurements will be discussed under vaporization studies in the next report.

For additional vaporization studies, it is desirable to synthesize mixtures with a well-defined melting point. It is necessary to use invariant melts for this purpose. The approximate composition of several such melts are given in Table 1. Compositions of these and other invariant melts will be reported with improved accuracy, pending full reduction of EDX data.

Table 1. Approximate Compositions of Selected Invariant Melts, System K_2O-CaO-Al_2O_3-SiO_2 (wt %).

Solids Present at Melting	K_2O	CaO	Al_2O_3	SiO_2
$KAlSiO_4/CaSiO_3$	11.7	25.7	19.2	43.5
$Ca_2Al_2SiO_7/CaSiO_3/CaAl_2Si_2O_8/KAlSi_2O_6$	6.0	30.3	25.4	38.4
$KAlSiO_4/KAlSi_2O_6/Ca_2Al_2SiO_7/CaSiO_3$	10.5	25.5	24.0	40.0
$Ca_2Al_2SiO_7/KAlSiO_4/KAlSi_2O_6/CaAl_2Si_2O_8$	11.5	17.6	33.7	37.2
$Ca_2Al_2SiO_7/Ca_3Si_2O_7/CaSiO_3/KAlSiO_4$	6.5	40.1	17.1	36.4
$KAlSiO_4/Ca_2Al_2SiO_7$	11.8	23.6	37.4	27.2

2. System K_2O-CaO-FeO_x-Al_2O_3-SiO_2

The effect of a slag coating on the electrical performance of the generator in open cycle coal-fired MHD systems continues to receive a substantial amount of attention. The problems associated with the behavior of slag in downstream components, and with the recovery of potassium seed captured by slag areno less significant in the operation and design of economical MHD systems. A quantitative knowledge of slag properties appears to be essential for several aspects of MHD research and development.

In an earlier paper[1] the available data on MHD channel slag compositions were summarized and working models were proposed for the bulk composition of slags produced by MHD combustion of typical subbituminous ("Western") and bituminous ("Eastern") coals. Vapor pressure measurements were reported for these two synthetic slags. The present paper is a continuation of this work, and here are described the results of exploratory phase equilibrium studies on the model slags. Also presented is an attempt to make meaningful generalizations and extrapolations through theoretical modeling of this experimental data. It is hoped that ultimately the otherwise intractable complexities inherent in the physical chemistry of MHD slag will become better understood so that reliable prediction and control of viscosity, electrical and ionic conductivity, seed retention, melting and crystalliztion behavior, corrosiveness, and other compositionally dependent properties will be possible.

In preparation for the development of a predictive model for immiscible K_2O-CaO-FeO_x-Al_2O_3-SiO_2 liquids, theoretical manipulations were begun of data taken previously (ref. [1]) on compositions of melts coexisting with $KAlSiO_4$ [2] for bulk compositions modeling "Eastern" and "Western" channel slag. It is expected that these results will be presented at the 7th International MHD Conference. The following paragraphs are excerpts from a paper submitted to that conference.

The ideal solution provides a useful starting point for any modeling effort. One form of the ideal solution equation for binary crystal/liquid equilibrium in system A-B is:

$$-\ln X_B^{melt} = -\ln X_B^{xl} + \frac{\Delta H_B^{fusion}}{R}\left(\frac{1}{T} - \frac{1}{T_B^{fusion}}\right)$$

where X_B^{melt} and X_B^{xl} are the mole fractions of component B in coexisting liquid and crystal, ΔH_B^{fusion} is the enthalpy of fusion of pure crystalline B, T_B^{fusion} is the melting point, R is the gas constant, and T is the temperature in degrees kelvin. It can be shown that this relation applies as well to crystal/liquid equilibria in multicomponent systems, In performing this calculation for the "Western" melts of ref. [1], the relatively small amount of iron in the residual melts may be assumed to be in the ferrous state. Sample calculations indicate that for purposes of this paper the above assumption is not likely to result in significant changes in the results of theoretical manipulations or their interpretation (for the "Eastern" melts this is emphatically not true).

The ideal solution calculations include the 85 mol % purity of the crystals involved, the heat of fusion used by Spencer et al. [3], and an assumed congruent melting point of 2058K. The resulting curve is shown in Figure 3a. If the precipitation of $KAlSiO_4$ is assumed to be defined by

$$(KAlSiO_4)^{xl} = 1/2(K_2O)^{melt} + 1/2(Al_2O_3)^{melt} + (SiO_2)^{melt}$$

so that

$$a^{ideal,\ melt}_{KAlSiO_4} = 8(X^{melt}_{K_2O})^{1/2}\ (X^{melt}_{Al_2O_3})^{1/2}\ (X^{melt}_{SiO_2})$$

then the calculated activities in Figure 3a are produced from compositional data in ref. [1]. The agreement between predicted and measured activities is thus not good, if the observed activity is defined in this way.

Some success in explaining the non-ideality of silicate melts has resulted from application of polymer theory. According to the model proposed by Toop and Samis [4], polymerization reactions may be summarized in quasichemical form by:

$$2O^- = O^{2-} + O^\circ$$

where O^{2-}, O^- and O° represent free oxide ions, non-bridging oxygens and bridging oxygens respectively. An equilibrium constant, k, can be defined accordingly. Values of k from the literature [4,5], with a temperature dependence assumed similar to that of the $FeO\text{-}SiO_2$ system [6] have been combined in the present work to calculate the distribution of quasichemical oxygen species in the melts of ref. [1]. A correction for standard state differences, in proportion to the ion field strengths of Ca^{+2}, Fe^{+2}, and Mg^{+2} has been applied [7]. Otherwise values of K for Fe^{+2} and Mg^{+2} are assumed equal. In these and subsequent calculations $KAlO_2$ and SiO_2 are considered as substituting ideally in the polymer network [8]. By solving the following equations, the number of moles, n, of O^-, O°, and O^{2-} per mole of melt may be found, where X is the mole fraction of $(SiO_2 + KAlO_2)$:

$$(8X - 8X^2)n^2_{O^-} + (-2X - 2)n_{O^-} + (1 - 4k) = 0$$

$$n_{O^\circ} = \frac{4X - (n_{O^-})}{2}$$

$$n_{O^{2-}} = (1 - X) - \left(\frac{n_{O^-}}{2}\right)$$

Results of this series of calculations for the melts of ref. [1] show marked increase in polymerization with increasing $(KAlO_2 + SiO_2)$, as indicated by the increased O° content of the melt. The free oxide ion content is, as would be expected, very low for all compositions.

Fraser [7] has modified the theory of Huggins [9] to allow prediction of the proportions of five basic SiO_4 structural units present in the melt using the quasichemical species of the Toop-Samis model. Structural units are indicated schematically by numbers in parentheses which give the number of non-bridging oxygens. Thus $SiO_4(0)$ represents a structural unit of the infinite framework, while $SiO_4(4)$ is the independent SiO_4 tetrahedron. Results of calculations for the residual melts show that only the $SiO_4(0)$ and $SiO_4(1)$ units increase in abundance with increasing mole % $(KAlO_2 + SiO_2)$, and hence, with increasing temperature. If an ideal activity is defined according to

$$a_{KAlSiO_4}^{ideal,\ melt} = 4\ (X_{KAlO_2}^{melt})\ (X_{SiO_2}^{(0),\ melt})$$

where $X_{SiO_2}^{(0),\ melt}$ is the mole fraction of $(KAlO_2 + SiO_2)$ in the melt present in the form of $SiO_4(0)$ structural units, or structons [9], then the calculated points in Figure 6b result, giving substantially lower activities than those predicted. However, if the calculation, is completed according to

$$a_{KAlSiO_4}^{ideal,\ melt} = 4\ (X_{KAlO_2}^{melt})\ (X_{SiO_2}^{(1),\ melt})$$

then the calculated $KAlSiO_4$ activities for the "Western" melts agree very well with those predicted from ideal solution theory, as shown in Figure 3c. It is suggested that while $SiO_4(0)$ is the structural unit most similar to the $KAlSiO_4$ structure, $SiO_4(1)$ has a non-bridging oxygen essential for reaction and therefore is the melt structural unit involved in the precipitation equilibrium. The result of this calculation may be taken as evidence that $KAlO_2$ and SiO_2 do indeed mix in a near ideal fashion in the polymer network; that $KAlO_2$ in all sites in the polymer network is of nearly equal reactivity; but that it is the degree of polymerization of the silica within the polymer network which determines the precipitation reaction of $KAlSiO_4$.

The quasichemical polymerization model can also be used to calculate the free energy of mixing for "Western" melts (Figure 3d) according to the following equation:

$$\Delta G_{mixing} = \frac{n_{O^-}}{2}\ RT \ln k$$

A nearly flat curve results in support of the stability of these melts with regard to unmixing. Note, however that the $a^{melt}_{KAlSiO_4}$ vs temperature data show irregularities between 1350 and 1550°C. This may be an indication of the misicibility gap known to occur a short distance away in compositional space, at the site of the "Eastern" bulk composition.

The approach has also been extended to results of experiments on the "Eastern" iron-rich bulk composition of ref. [1]; however, the liquidus surfaces are apparently too complex to be modeled by simple precipitation reactions of the type outlined above, which worked reasonably well for the iron-poor, calcium-rich "Western" composition. This probably is the result of non-ideal entry of ferric iron into the silicate polymeric framework. Nonetheless the quasichemical approach seems to work well for description of the free energy of mixing, where it is possible to ignore specific polymeric interactions. To perform free energy calculations on "Eastern" melts, a series of compositions along a vector through seven-component space have been chosen. The vector is defined by the two immiscible melts coexisting at 1550°C (ref. [1]) whose compositions are given in Table 2. Ferric iron and Al_2O_3 have been included in the calculations by assuming equilibrium constants appropriate for relatively undissociated oxides (3.81 and 4.38, respectively). Results of these free energy calculations are shown in Figure 7, at a series of Fe^{+3}/Fe^{total} ratios. It has been assumed for purposes of these calculations that this ratio is the same in both melts of the immiscible pair. Figure 7 illustrates the rather dramatic effect of Fe^{+3}/Fe^{total} on the mixing properties of these iron melts. A large region of liquid unmixing for more oxidized melts is predicted. Composition of predicted and observed melts can be compared in Figure 7b, and it can be seen that by judicious choice of equilibrium constants and assumed Fe^{+3}/Fe^{total} reasonable agreement can achieved through use of the quasichemical model.

The quasichemical approach offers hope in the development of a quantitative model for description of slag behavior under MHD conditions Further progress will require knowledge of how entry of ferric iron into the melt affects polymerization reactions.

Table 2. Compositions of Coexisting Immiscible Liquids at 1550 °C, "Eastern" Bulk Composition (mole %).

	Silica-rich (S)	Iron-rich (F)
SiO_2	45.87	25.07
Al_2O_3	15.58	9.00
FeO_x	18.57	49.85
CaO	4.92	6.88
MgO	1.30	1.32
K_2O	13.76	7.88
	100.00	100.00

Plans: Continue vapor pressure measurements on selected portions of the K_2O-Al_2O_3-CaO-SiO_2 system.

Preparation of melts with known phase equilibrium behavior for vaporization studies in the system K_2O-CaO-Al_2O_3-SiO_2 will continue. Studies of subsolidus equilibria in the system will resume, and will concentrate upon equilibria involving $KAlSiO_4$, Ca_2SiO_4, K_2CaSiO_4 ($KAlO_2$-K_2CO_3) ss and related phases.

References

1. W. R. Hosler, T. Negas and S. J. Schneider. Development. Testing and Evaluation of MHD Materials, NBS reports prepared under DoE Contract EA-77-A-01-6010, April-June 1978 and July-September 1978.

2. L. P. Cook, R. S. Roth, H. S. Parker, and T. Negas, Am. Mineral., 62 1180 (1977).

3. F. E. Spencer, J. C. Hendrie, Jr., and D. Bienstock, Sixth Int. Conf. on MHD Electrical Power Generation, 2 181 (1975).

4. G. W. Toop and C. S. Samis. Trans. Metal. Soc. AIME, 224 878 (1962).

5. C. K. Masson, I. B. Smith, and S. G. Whiteway, Canad. J. Chem., 48 1456 (1970).

6. P. A. Distin, S. G. Whiteway, and C. R. Masson, Canad. Metal. Quart., 10 73 (1971).

7. D. G. Fraser, p. 301-325 in: D. G. Fraser, (ed)., Proc. NATO Adv. Study Inst., Oxford, England, 1976 (1977).

8. F. J. Ryerson and P. C. Hess, Geochim. et Cosmochim. Acta., 42 921 (1978).

9. M. L. Huggins, J. Phys. Chem., 58 1141 (1954).

10. E. R. Plante and L. P. Cook, Proc. 17th Symp. Eng. Aspects MHD, Stanford, C.1.1. (1978).

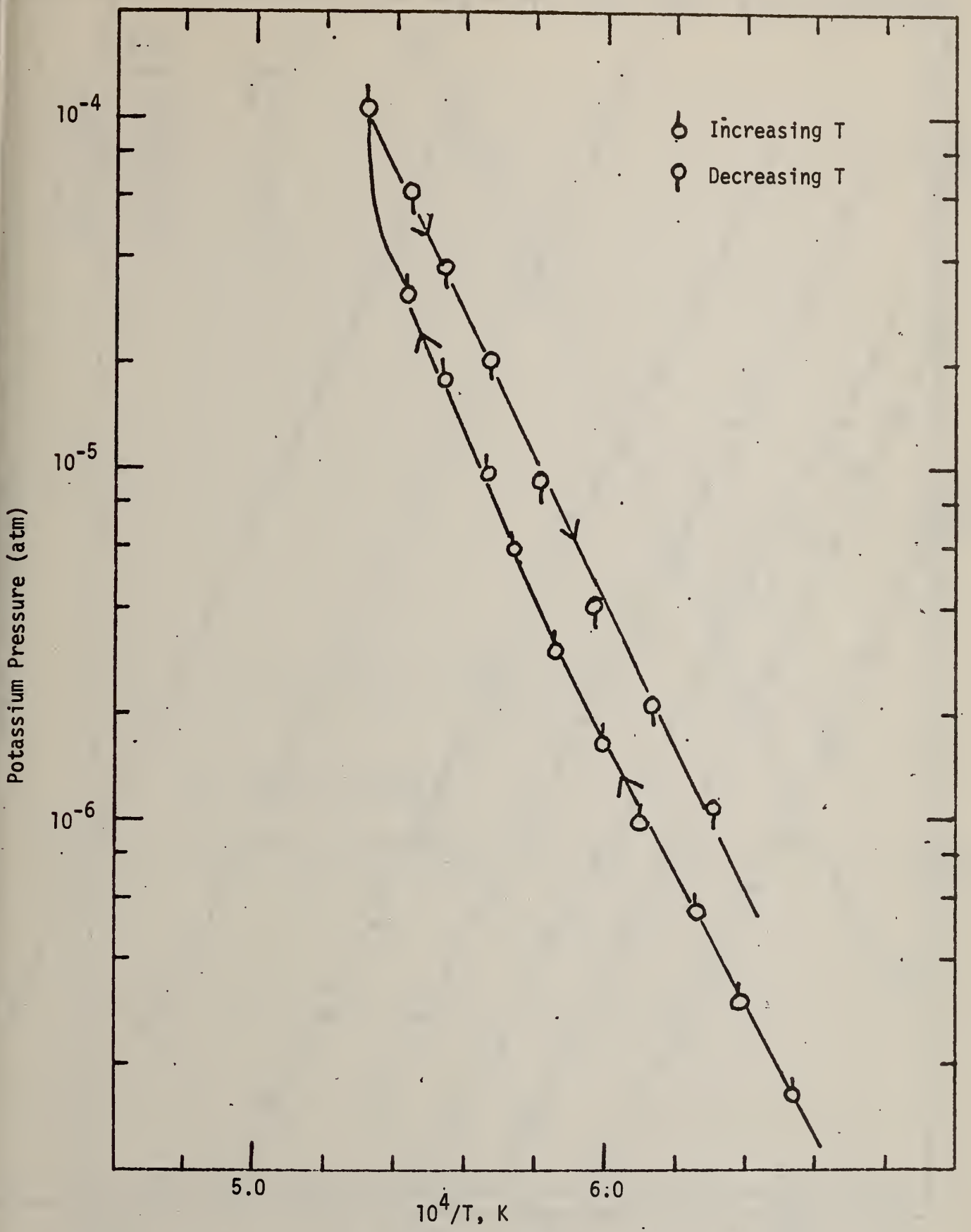

Figure 1. Non-equilibrium effect in the vaporization of $KAlSiO_4$ due to low concentration of $KAlSiO_4$ and partial melting.

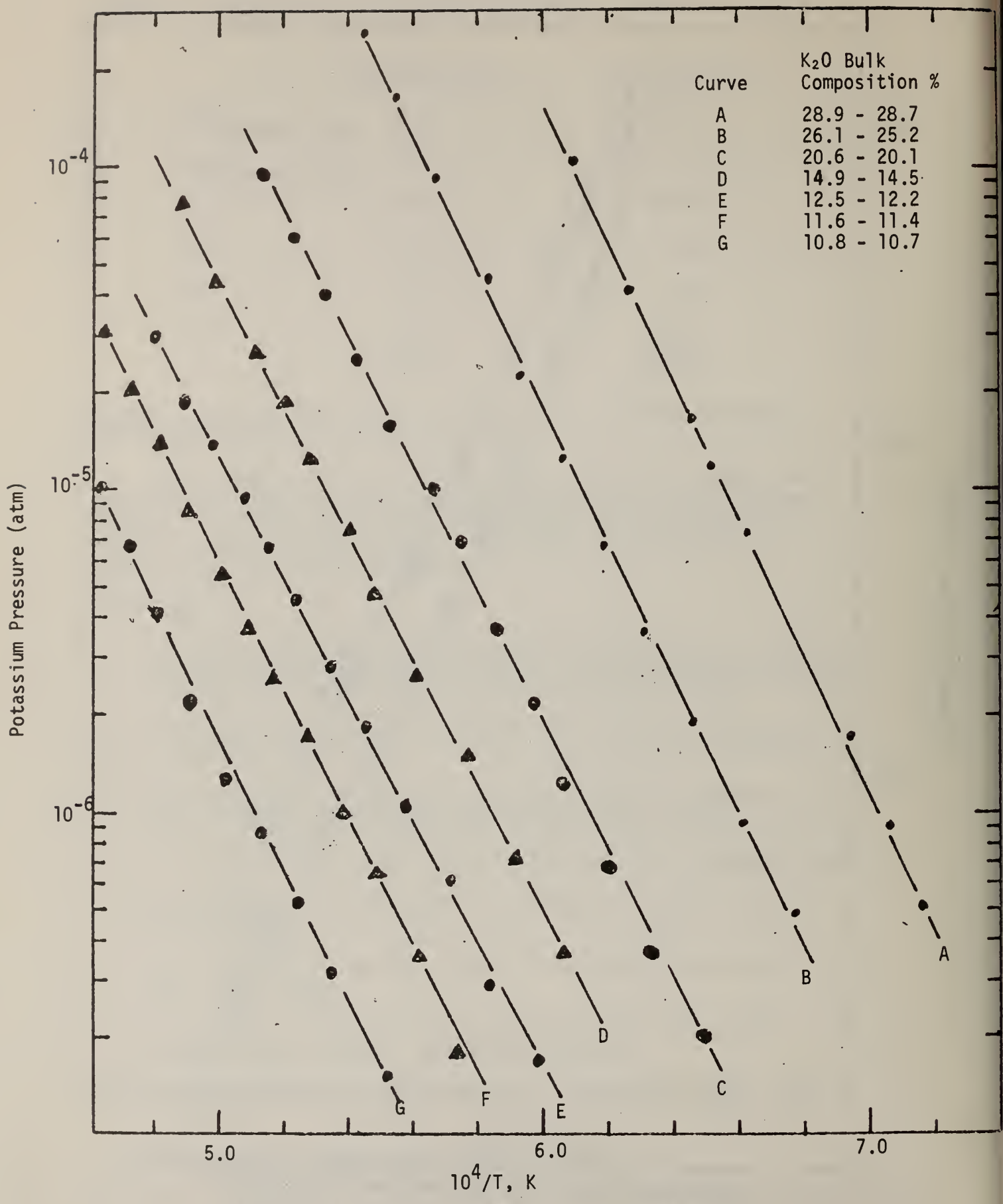

Figure 2. Selected K vapor pressure data of $KAlSiO_4$ as a function of 1/T and bulk composition.

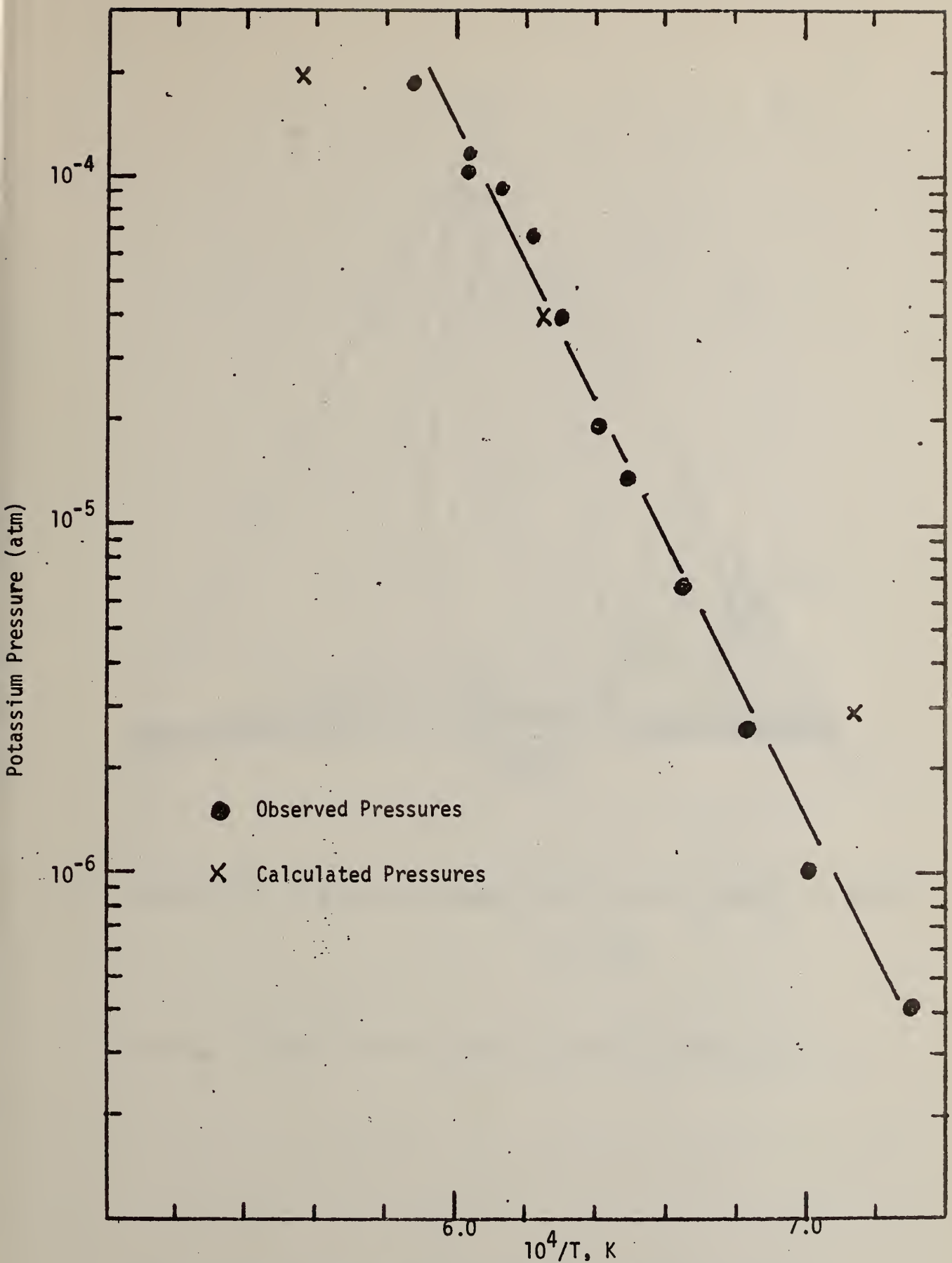

Figure 3. Vapor pressure of K produced by reaction of $KAlSiO_4$ with Ca_2SiO_4.

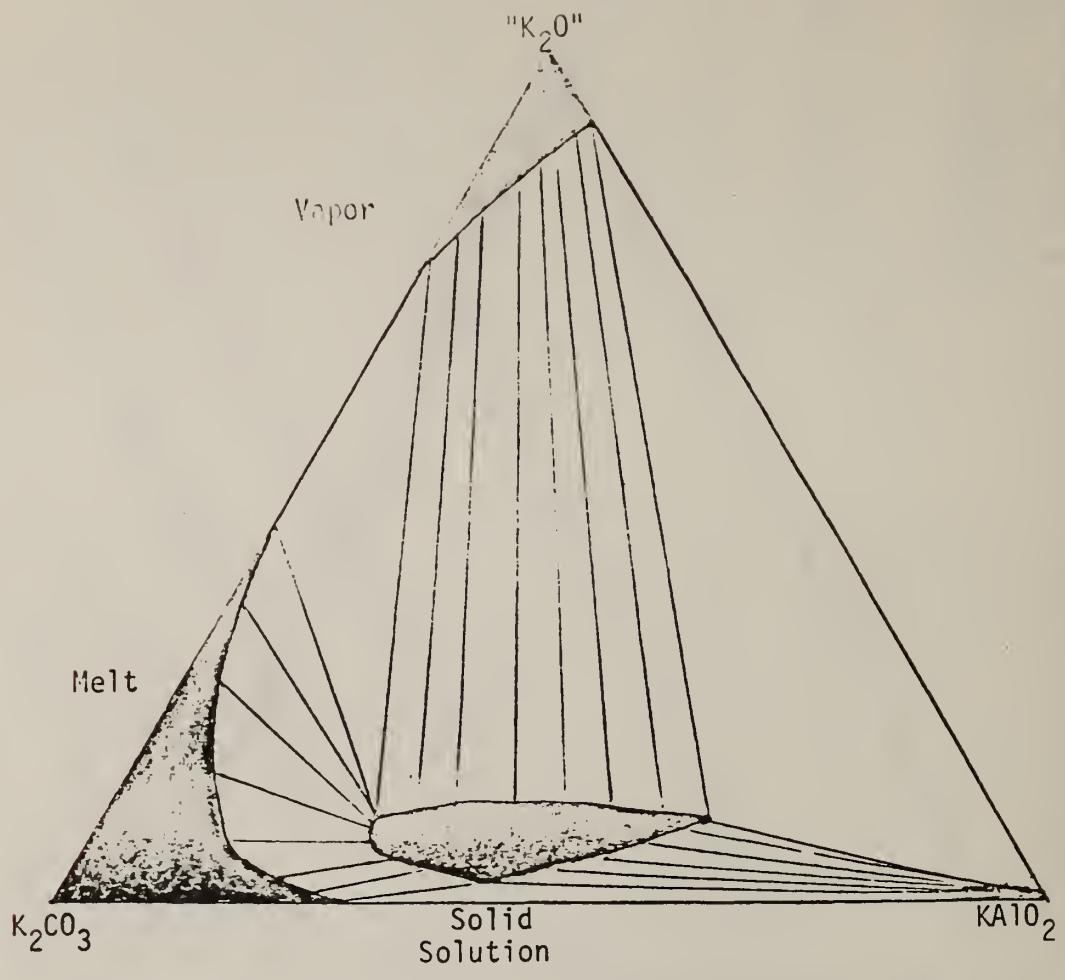

Figure 4. Schematic phase diagram showing stability of ($KAlO_2$-K_2CO_3) ss.

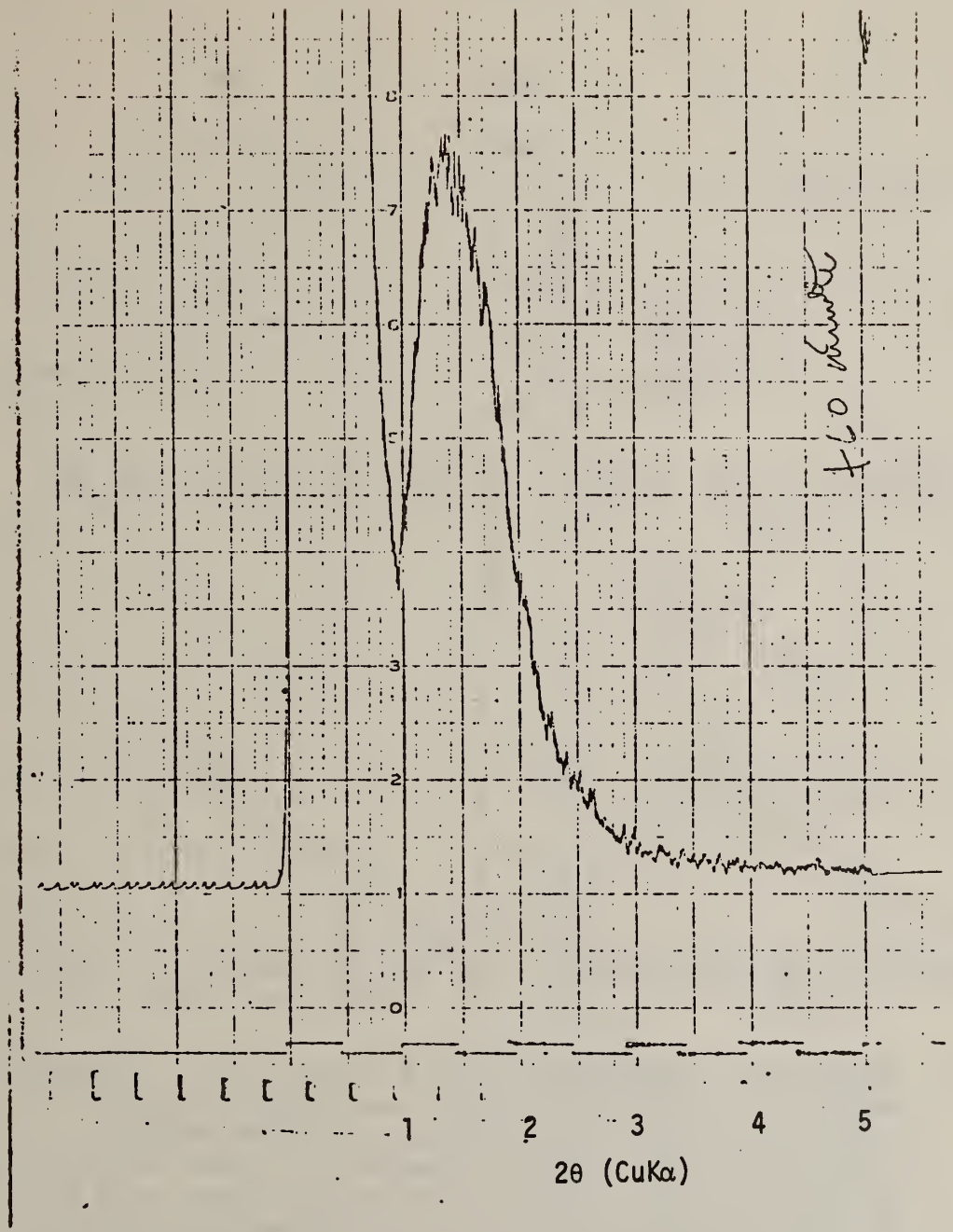

Figure 5. Low angle portion of powder pattern of ($KAlO_2$-K_2CO_3) ss.

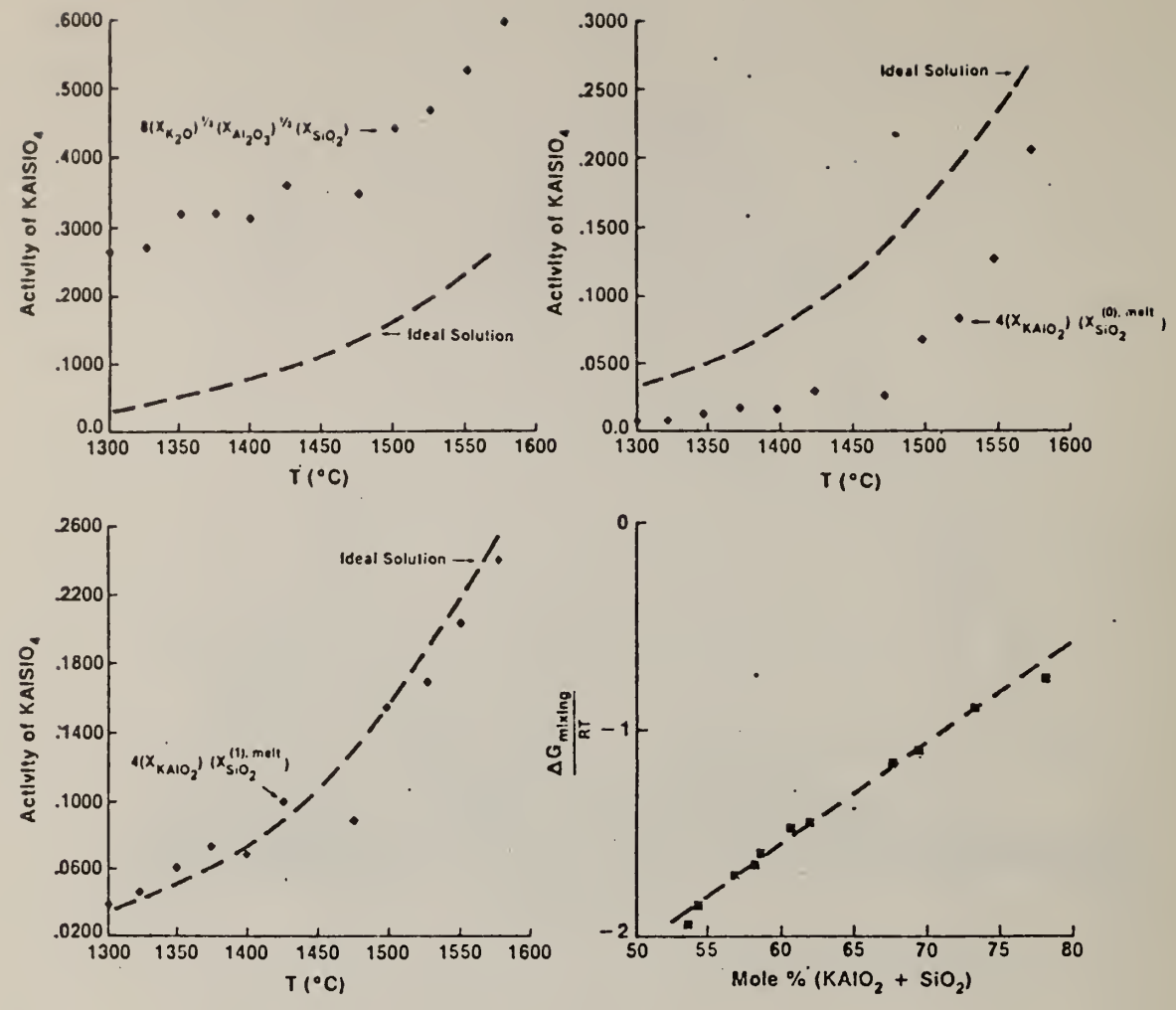

Figure 6. Theoretical manipulations of melt data in ref. 1, "Western" model slag. a) Ideal solution freezing point depression compared with activity of $KAlSiO_4$ calculated from precipitation of the oxides. b) Comparison of ideal $KAlSiO_4$ activity with that calculated for precipitation using $SiO_4(0)$ structons. c) Comparison of ideal activity with that predicted from precipitation by $SiO_4(1)$ structons. d) Calculated free energy of mixing for "Western" residual melts as a function of mole % ($KAlO_2$ + SiO_2).

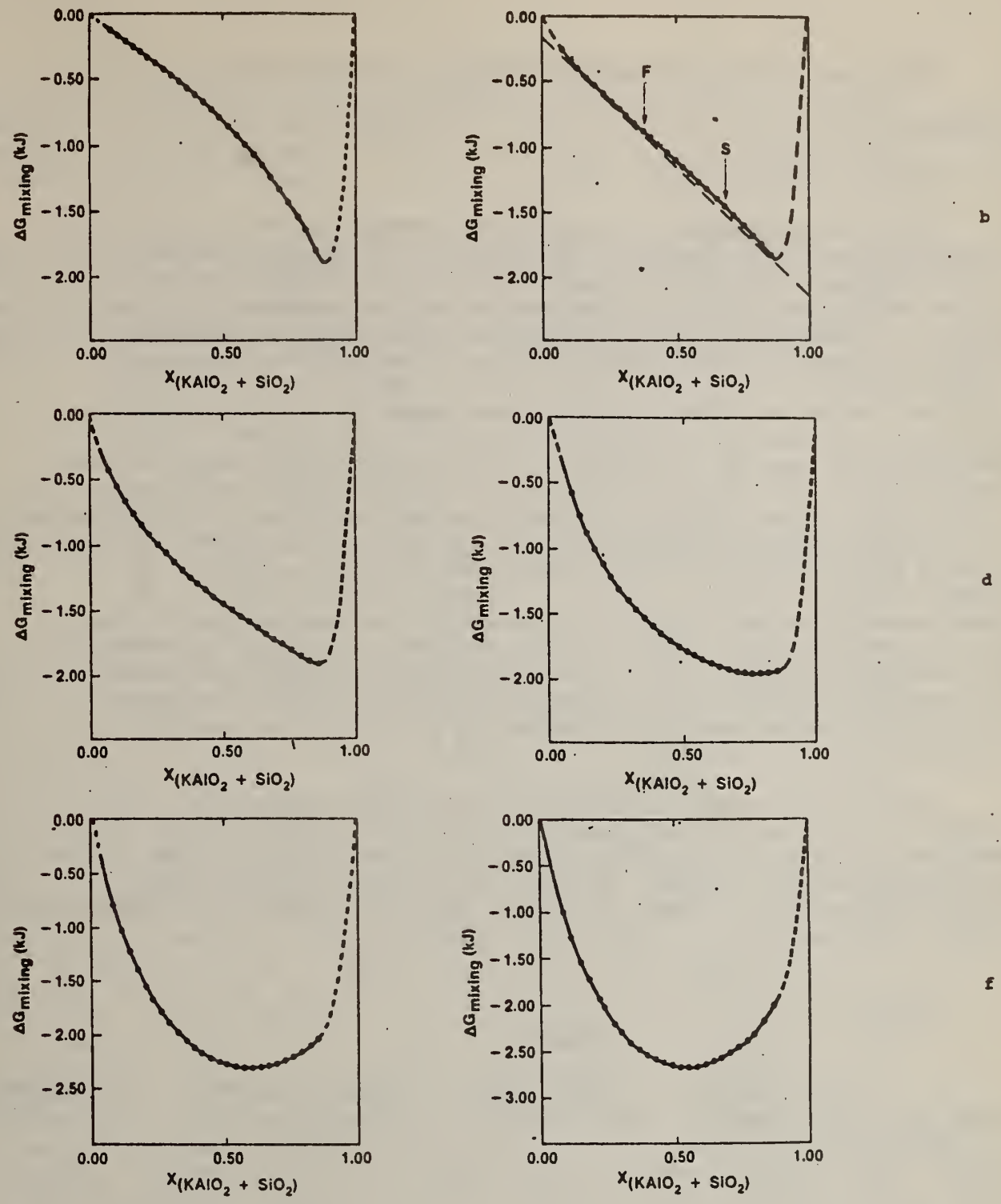

Figure 7. Calculated free energy of mixing along a compositional vector passing through the compositions of immiscible melts, "Eastern" bulk composition (see Table 2). Calculations assume 1550°C and Fe^{+3}/Fe^{total} = 0.3000 (Fig. 7a), 0.2500 (Fig. 7b), 0.2000 (Fig. 7c), 0.1500 (Fig. 7d), 0.0909 (Fig. 7e) and 0.0476 (Fig. 7f). Tangency is drawn in Fig. 7b to facilitate comparison with observed immiscibility (melts S and F). These free energy curves have been drawn by computer to fit calculated points using a piecewise cubic interpolating polynominal. Dashed portions of the curves lie slightly off the compositional vector.

2. Electrical Conductivity and Polarization (W. R. Hosler)

Progress

a. Electrical Conductivity of $YCrO_3$

Initial measurements of the pressure dependence of the electrical conductivity of $YCrO_3$ doped with 5% calcium on the yttrium site have been completed. There has been some difficulty in establishing the oxygen partial pressure in the sample chamber that corresponds to the oxygen partial pressure in the flowing gas where oxygen/nitrogen gas mixtures are used. This difficulty arises because of the large sample chamber (1200 cm^3) originally filled with air which must be swept out with the flowing environment gas of chosen composition. True oxygen pressure dependence of the conductivity can only be measured after the environment gas has been completely changed in the sample chamber. This requires times in excess of 4 hours with a flow rate of 450 cm^3/minute. In contrast, however, for those atmospheres where very low oxygen pressures are obtained by the reaction $2H_2 + O_2 \rightarrow 2H_2O$ such as is obtained using forming gas (95 nitrogen to 5 hydrogen), the low oxygen pressures are obtained quickly (1 hour or less) in the environmental chamber. The measurements have been completed in atmospheres containing about 5 ppm O_2 in N_2 and in an atmosphere of 10^{-25} atmosphere oxygen as indicated on a zirconia tube oxygen sensor gauge based on the Nernst-Einstein relation. (Intermediate oxygen pressures between 5×10^{-6} and 10^{-25} atmospheres will be obtained in future experiments by mixing the 5 ppm gas with forming gas.)

Table 1 gives values of conductivity and soak temperatures. The conductivity values are those taken at the end of the soak period, but data were taken at 5 to 10 minute intervals during the soak period, before equilibrium was established. The order in the Table is the sequence in which the data were taken. As can be seen, the scatter in the conductivity data is quite large.

Table 1

Temp. °C	O_2 pressure (atmos.)	Conductivity σ $(ohm\text{-}cm)^{-1}$	Total flow time before meas. (hr)	Soak Time at T. (hr)
1300	5×10^{-6}	2.9	18	18
1500	"	3.12	20	2.5
1400	"	3.05	23.5	3.0
1400	5×10^{-25}	1.05	11.5	11.5
1600	"	1.30	14.5	3.0
1500	"	1.05	16	1.5
1400	"	0.92	17	1.0
1300	"	1.04	36.5	19.5
1600	"	1.02	45.0	8.5
1500	"	0.88	56.5	11.5

There has been some difficulty in preparing good single-phase material. Possibly, as a result of this multi-phase condition, samples oxidized after having been prepared in a highly reduced state sometimes exhibit small hairline cracks. These cracks will cause erratic results in the conductivity values.

$YCrO_3$, doped with Ca or Mg in a highly reduced state, is very hard and it is difficult to saw or drill with diamond tools. In the oxidized state, however, it is relatively soft and sometimes fragile and breaks easily upon handling. More work must be done on phase composition and microstructure and their relation to oxidation/reduction conditions before final work can continue on the electrical conductivity measurements.

b. Electrochemical Effects of Slag-Electrode Interfaces

An electrochemical cell, consisting of four platinum probes immersed in Bow, NH slag containing 20% added K_2SO_4, was constructed. This cell was heated to 1250 °C and subjected to a constant applied voltage mode test where the voltage was reversed periodically during the course of a 2-1/2 hour run. Voltages were monitored on all probes during the test.

Figure 1 is a radiograph of the electrochemical cell, while Figure 2 shows the voltage on the various probe sets as a function of time. A constant 31 volts was maintained between the top and bottom probes and this resulted in an initial current, after each current reversal, of 60 to 100 mA, which drops off with time as shown in the figure. The current was reversed at 5 minute intervals (after a initial interval of 2 1/2 minutes) over a period of 2 1/2 hours. Only 23 1/2 minutes of the data are shown, but the remaining data over the entire experiment period are repetitive. It can be readily seen that, for example, when the top probe is positive (anode), as in periods A, C, and E, nearly all the potential drop in the cell is across the I_T ρ_T set of probes, after a few minutes operation, while the voltage across I_B ρ_B (I_B cathode) is low. Current reversal then produces a large potential drop at the I_B ρ_B probes and a small voltage at the I_T ρ_T probes. In previous experiments (see QR Sept.-Dec. 1977), some iron depletion was observed in the anode area just outside the platinum electrode in an electrochemical cell run for a period of 20 hours at 1400 °C. At the same time, definite enrichment of iron was observed at the cathode slag-electrode interface. Cadoff[1], in electrochemical work on slag-electrode reactions, shows that in cells designed for static slag (non-flowing), the potential buildup of the cell is due to the accumulation of electrically resistive ions at the slag/anode interface. Koester et al.[2] has shown that the critical potential for arcing or breakdown is higher for AISI 1018 steel than for nickel or Type 304 stainless steel. This may be due to the supply of iron from the anode electrode alleviating the usual iron poor (or silica rich) area just at the anode/slag boundary, usually associated with an electrode material not containing iron. This experiment demonstrates that this potential buildup is relatively rapid and is associated with the slag-anode interface. At the same time, the conductivity of the bulk slag remains unchanged since the potential on the probes ρ_T ρ_B drops off in proportion to the drop off in the primary current while the applied voltage is constant.

A second experiment on this same cell was performed using a constant current (30 mA) mode but reversing the current periodically (5 minute intervals). Figure 3 shows that data obtained over a 20 minute period in the experiment. Although the experiment was run for 1 1/2 hours, only slight changes were observed with time on reversal of the current. Breakdown in the current conducting mechanisms, after a current reversal, appears to occur earlier, when the I_B probe is an anode as in period B and D (1.5 to 2.0 minutes), than when the I_T probe is an anode as in periods A and C (4 to 5 minutes). Since the experiment was run at 1250 °C, there could be a difference in the oxidation state of the iron between the top and bottom of the cell and this might cause a difference in the breakdown potential when the anode is at the bottom of the cell (away from ambient atmospheres). Also, with the top of the cell as anode for a 5 minute period followed by a 5 minute period with the current off (these periods not shown in figure), the cell returns to its original state;, i.e., the potentials are distributed evenly along the length of the cell, showing that any depletion layer has been repaired. However, with the bottom of the cell as anode, and the same procedure followed, the depletion layer is not repaired completely even after a period of 50 minutes. A measurement of all probe voltages with current off yields zero potential indicating that there is no measurable battery effect present. In the constant current mode, the high potential develops between the anode and its adjacent conductivity probe, as was also observed in the constant voltage mode. Breakdown occurs also at the anode. The corresponding cathode potential decreases with time after a slight initial increase after reversal. The slag bulk conductivity decreased (potential on ρ probes increased) slightly during the course of the experiment which may be due to iron diffusion into the platinum electrodes.

Both of these experiments were done at a temperature (1250 °C) where the slag is very viscous and where there may be a combination of ionic and electronic (semiconductive) conductivity. If time permits, this experiment should be repeated at higher temperatures where the conductivity is believed to be largely ionic and due primarily to the movement of iron ions.[3]

c. Slag Electrical Conductivity

A sample of slag was made from the Bow, NH slag which contained an added 20% K_2SO_4, but now with an additional 20% of Fe_2O_3. Figure 4 shows the conductivity data as a function of temperature in an air atmosphere. The sample was heated to 1500 °C and held at that temperature until the conductivity became constant as a function of time (< 1/2 hour). It was then cooled as rapidly as possible in the furnace to 900 °C which required a period of 24 minutes. The temperature was then lowered slowly to 500 °C. The data shown in Figure 4 were taken with temperature increasing; conductivity versus time was monitored to obtain maximum or minimum conductivity values. The conductivity is higher in this sample than in its companion sample without the added iron, shown in QR July - Sept., 1979. The conductivity near the maximum at 1200 °C is approximately a factor of 2 higher in this sample with the added iron when long cool down times through this temperature range allow for crystallization of the slag. X-ray diffraction measurements indicate that at

these conductivity maxima, the crystalline components of the slag are feldspar sesquioxide, and spinel solid solutions of undefined bulk compositions. It is not possible to deduce whether the conductivity is due to these crystalline phases or to an iron-rich glassy matrix likely to be surrounding the crystalline components. In the latter case, the conductivity would be predominantly ionic. However, polarization effects were not observed in this temperature range during the electrical measurement.

The conductivity in the higher temperature range above 1350 °C is a factor of 5 greater in this sample with added iron (24.2 w/o) than in the sample with no added iron (14.7 w/o). Capps[4] has shown that there is a decrease in slag viscosity with increased iron content and with decreased silica content. The relative silica content necessarily decreases with any added component other than silica itself. This disproportionate increase in conducitivity may be due to the viscosity decrease reflecting the validity of the Walden rule[5] i.e. $\eta \cdot \sigma = \text{const.}$ where η is viscosity and σ is the electrical conductivity for conducting ionic species (iron ions) in a molten glass.

The data reported in this work are repeatable with repeated treatments and form the basis of a systematic approach toward understanding the electrical conductivity in the coal slag which will coat the electrodes in an MHD generator.

Plans

The electrochemical experiments will continue with the experiments described in the report repeated at higher temperatures in order to determine the polarization and relaxation times associated with any depletion layer formed while the cell is carrying current.

Work on the slag electrical conductivity will continue also. Preliminary investigations indicate that adding iron as Fe_2O_3 or Fe_3O_4 to Bow, NH slag without potassium causes excessive frothing and that these additions can only be made in a highly reducing atmosphere. Additional transition metal dopings may be investigated in order to better understand the conductivity.

References

(1) Westinghouse Electric Corporation - Quarterly Report for the Period Oct. 1 to Dec. 31, 1977, Contract No. EX-76-C-01-2248.

(2) Electrical Behavior of Slag Coatings in Coal Fired MHD Concentrations, J. K. Koester, R. M. Nelson, 16th Symposium on Engineering Aspects of Magnetohydrodynamics, University of Pittsburg, Pittsburg, PA, May 16-18, 1977.

(3) Conductivity Mechanisms in Iron-Containing Slag, W. Hosler, G. White, and T. Negas - 7th International Symposium on MHD, M.I.T., Cambridge, Mass., June 16-20, 1980.

(4) Coal Slag Properties Related to MHD, W. Capps, Conference on High Temperature Sciences Related to Open-Cycle Coal Fired MHD Systems, Argonne National Laboratory, April 4-6, 1977.

(5) International Review of Science - Electrochemistry-Physical Chemistry Series Two, Volume 6, J. Bocknis, Editor, p. 290.

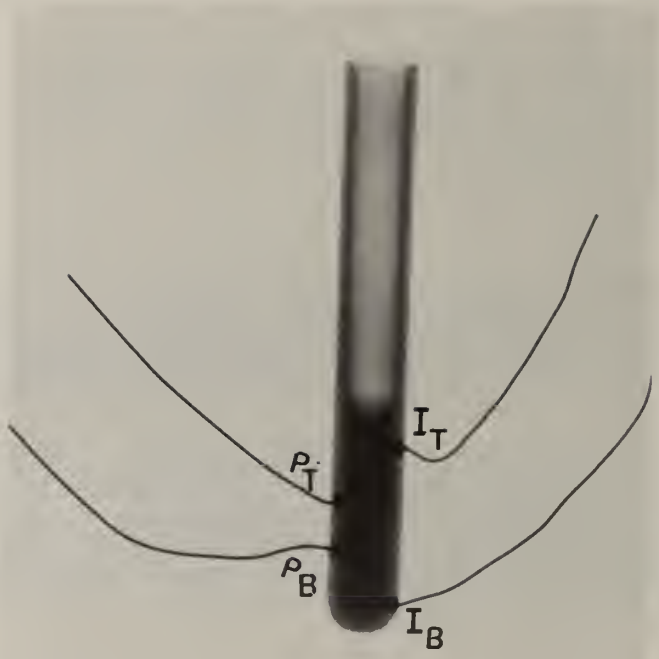

Figure 1. Radiograph of the electrochemical cell showing the arrangement of the platinum electrodes.

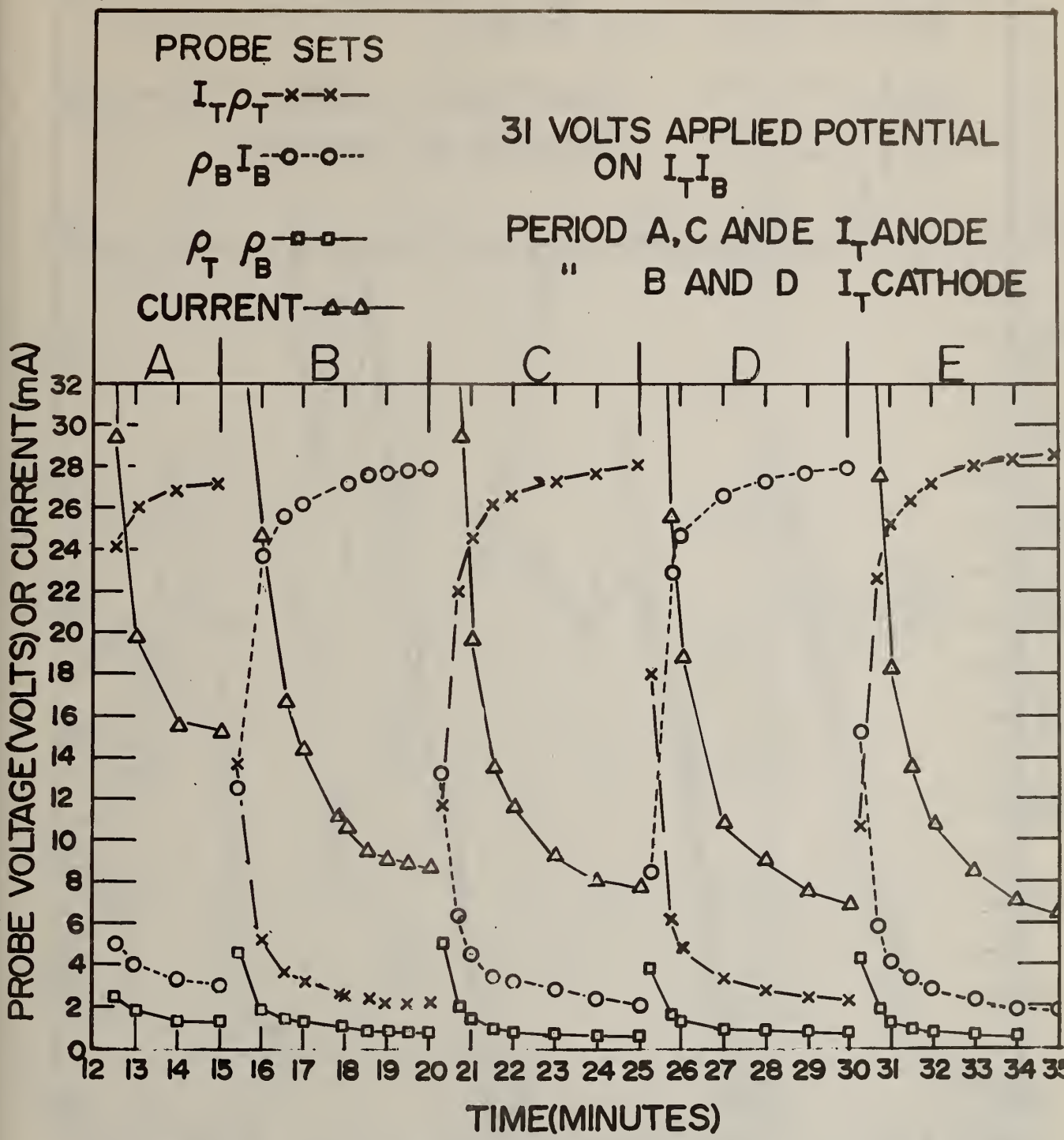

Figure 2. Probe set voltages and current as a function of time with periodic applied voltage polarity reversal. The applied voltage magnitude was constant during the run. Cell temperature 1250 °C.

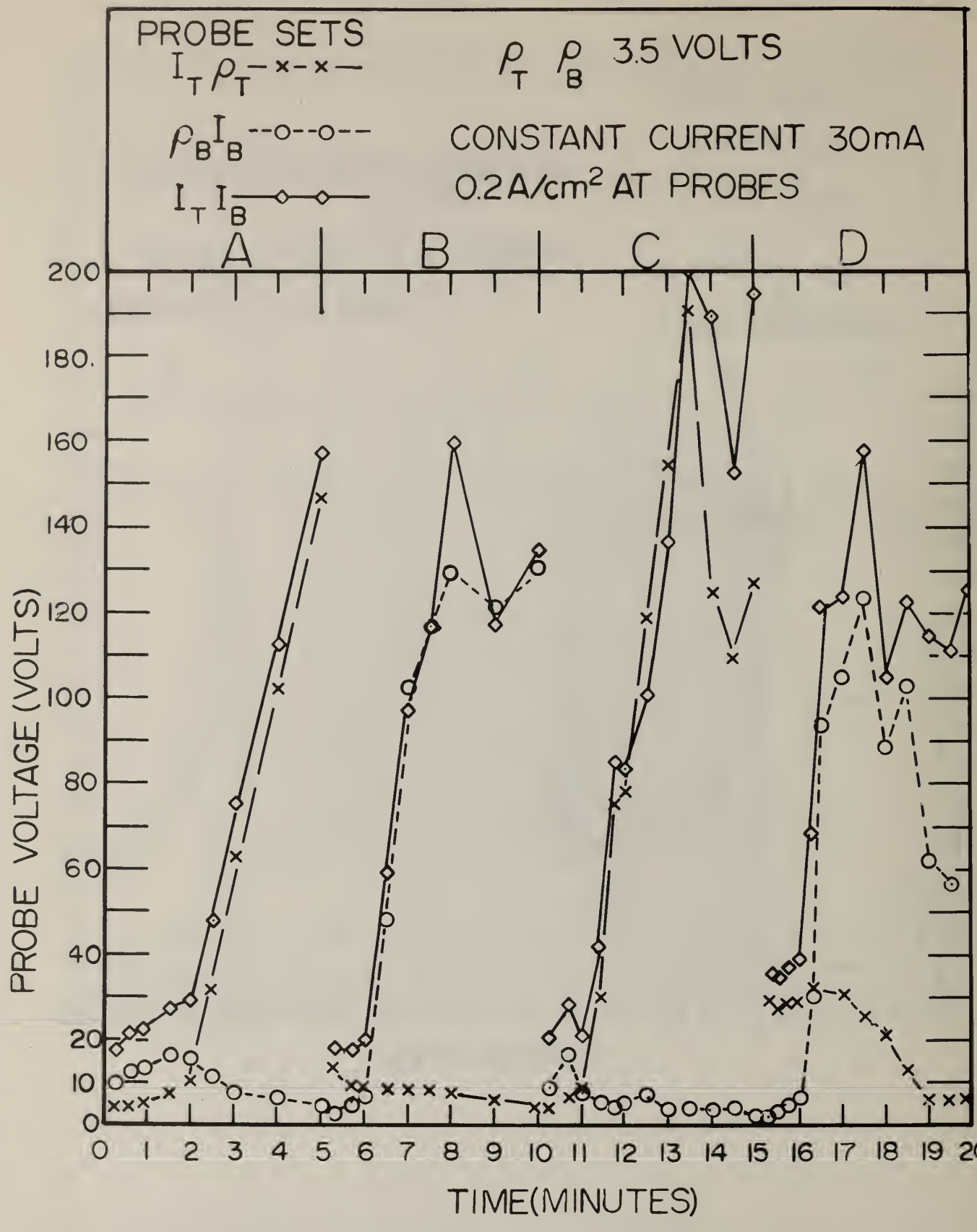

Figure 3. Probe set voltages as a function of time with periodic applied voltage polarity reversal. The current magnitude was constant during the run. During breakdown, recorded voltage magnitudes do not represent systematic cell behavior. Period A and C, I_T was anode. Period B and D, I_B was anode. Cell temperature 1250 °C.

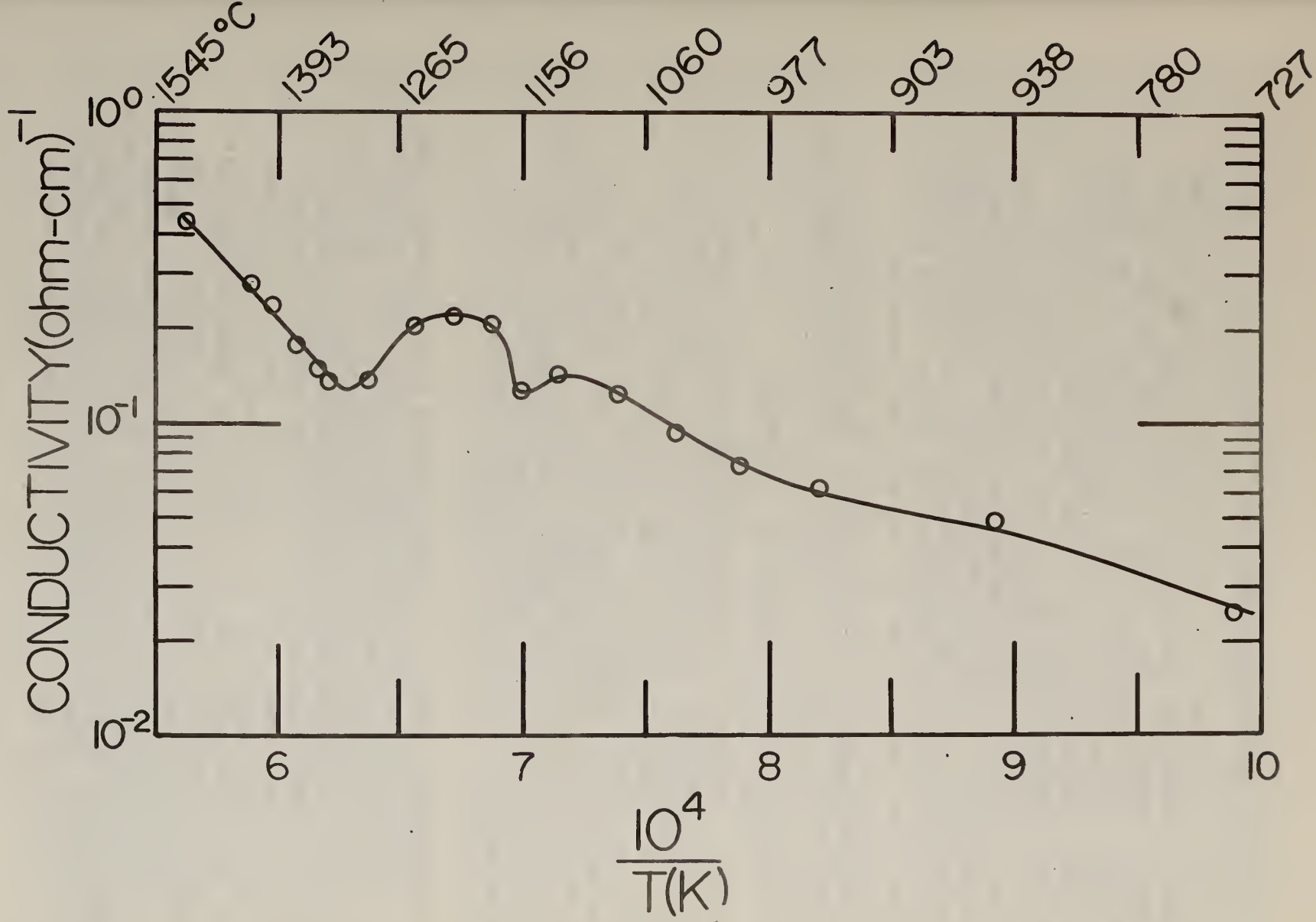

Figure 4. Electrical conductivity of Bow, NH slag with an added 20 w/o K_2SO_4 and with 34.6 w/o Fe_2O_3 (24.3 w/o Fe) as a function of temperature. These measurements were done in air.

3. Corrosion of Downstream MHD Components (J. Smit and C. D. Olson)

Progress: Tubular specimens of Type 316 and Type 304 stainless steel were exposed, under varied conditions, to K_2SO_4-seeded, oxygen rich, oxygen-propane hot gas streams. Following exposure, the specimens were analyzed using SEM, EDX and in some cases gravimetric techniques for indications of both incipient and gross corrosion. Test exposure time, excluding apparatus warm-up and cool down time, was 4 hours. Seeding with 250 grams of K_2SO_4 was effected during the first 25 minutes of that interval. Six stainless steel specimens were exposed under these general conditions with the tube temperature maintained at one of three levels: 400 °C, 500 °C or 590 °C. These temperatures were fixed by internal air cooling and were monitored by a Pt/Pt10%Rh thermocouple welded into the specimen wall at the mid length point. The specimens were seated in the test rig with the thermocouple located in the center of the hot zone and facing the gas stream. The gas stream temperature in the vicinity of the test specimen was held at approximately 1300 °C as indicated by a Pt/Pt10%Rh thermocouple.

A. SEM/EDX Analysis of the Metal-Deposit Interface

Metallographic specimens were prepared from three of the Type 316 stainless steel specimens, 1-6, 2-6, and 3-6, exposed at 590 °C, 500 °C and 400 °C, respectively. These sections were taken approximately 10 mm from the mid point position in the hot zone. To reduce the possibility of external contamination and hydration in the coatings formed on the tubular specimens during seeding, the specimens were removed from the test rig upon cool down to about 40 °C and encapsulated immediately in epoxy. The metallographic sections taken from the encapsulated tubular specimens were cut, ground and polished using non-aqueous media and were stored in evacuated desiccators prior to SEM/EDX analysis.

On all the specimens a compact, somewhat columnar deposit formed on the surface facing the gas stream. The thickness of this deposit varied slightly with tube temperature and is approximately 1.7 mm. A much thinner almost undetectable deposit, probably from fume, formed on the trailing surface. These deposits are in the 0.2 mm range. At the boundary, where the surface deposit and the fume deposit intersected a thicker drip zone formed; see Fig. 1, 2 and 3. The SEM micrograph, Fig. 4, shows a K_2SO_4 deposit on the leading surface of a Type 316 stainless steel tube held at 590 °C. This type of deposit is typical of that produced from K_2SO_4 seeding and was seen on specimens of Type 304 stainless steel tested previously under these conditions. EDX analysis indicates that potassium and sulfur is uniformly distributed through the bulk of the deposit. An SEM micrograph, Fig. 5, shows the top of the salt deposit with a fine whitish band on the surface. This band contains a higher proportion of potassium than the bulk of the deposit possibly due to vaporization of some sulfur at the deposit-gas stream interface.

The stainless steel deposit interface is seen in SEM micrograph, Fig. 6. Note that the adhesion is rather poor as epoxy fills a gap in the interface region, though this occurs after cooldown. A reaction area at the interface is shown in SEM micrograph, Fig. 7. At the metal edge, areas of low chromium and low nickel concentration are found dotted with regions of high nickel concentration, Fig. 7a - 7d. A loss of iron is also associated with these areas. At the deposit edge, concentrations of iron, chromium, potassium and sulfur are found indicating some degradation of the metal surface and formation of a reaction zone between the metal and the deposit, Fig. 7e - 7h. The SEM/EDX analysis seems to indicate a preferential leaching of the metal cations from the bulk material (Type 316 stainless steel) in a somewhat orderly fashion as in the case of Type 304 stainless steel. However, the extent of corrosion is not as great as in the case of Type 304 stainless steel. This is corroborated by wastage (weight loss) experiments also described in this report.

As found in previous specimens, though nickel loss is readily detected, its displacement to other areas is difficult to follow. Few areas are found where nickel has migrated even though its concentration is low. Fig. 8 shows a reaction area where low chromium and low nickel concentrations are found at the metal edge, Fig. 8a and 8b, and metal cations are found at the edge of the deposit, Fig. 8c - 8e. Migration of the iron, Fig. 9 , is farther back in the deposit and generally parallels previous results in which iron was preferentially leached out of the bulk stainless steel and into the deposit.

Fig. 10 shows a portion in the fume deposit area where the corrosion process seems to be evident. On the metal edge low nickel areas are found, Fig. 10a - 10c, while areas of chromium, iron, potassium and sulfur are found in the reaction zone. Again, nickel is the elusive element. Though it is found in low concentration in the reaction zone, it is not really found to have migrated into the deposit region.

At a lower temperature, 500 °C, corrosion is still observed in Type 316 stainless steel. Fig. 11 shows a region of corrosion at the metal-deposit interface. EDX analyses of the region, Fig. 11a - 11h, indicate areas of low metal cation concentration at the metal edge and metal cation migration into the deposit. The same can be said at the still lower specimen temperature of 400 °C but to a much lesser extent.

B. Metal Wastage Analysis

Weight loss determinations and tube surface examinations by SEM and EDX techniques were also made on Type 316 and Type 304 stainless steels. Three specimens, one of Type 316 stainless steel, specimen 4-6, and two of Type 304 stainless steel, specimens 13-4 and 14-4, were weighed prior to exposure at tube wall temperature of 590 °C, 590 °C and 400 °C,

respectively, under the general conditions as described in the first paragraph of this report. In these cases, after extraction from the test rig, the entire specimen was rinsed in warm water and subsequently cleaned in 10% HNO_3 at 50 °C for 20 minute cycles in an ultrasonic bath until constant weight was obtained. In each case the second cleaning cycle resulted in no further detectable weight change. The differences in weight (weight loss) are attributed to loss of metal (wastage) from the specimen; see Table 1. Fig. 12, 13 and 14 show the stainless steel tubes after exposure and cleaning. After weighing, sections were taken from each tube for SEM/EDX analysis.

Fig. 15, a micrograph of specimen 4-6, shows areas of pitting and wastage. Fig. 16, along with the EDX analysis, indicates regions of cation migration and concentration. There seems to be no general trend towards concentration of any metal cation; however, there seems to be a general trend towards lower nickel concentrations. To see if these conclusions were reasonable, another area, shown in Fig. 17, was examined. Fig. 18 shows again areas of low nickel, Fig. 18a and 18b, but also regions of high nickel, Fig. 18c, along with areas of other metal cation concentration. However, the high nickel regions are generally isolated and not in sufficient number to account for all the low nickel regions. Although the wastage (weight loss) of this sample was minimal, the nickel concentration tends to be lower than that of the bulk stainless. It is possible that this occurs because the nickel is being attacked and lost through some volatile chemical reaction or it may be that there is a formation of a higher chromium, iron layer that has migrated upwards covering the nickel. In either case, lower nickel would be observed.

In samples 13-4 and 14-4 a comparison evaluation can be made of the same type of stainless steel exposed at two different temperatures. The greatest change in weight (wastage) was observed in sample 13-4, while a minimal amount was lost in sample 14-4; see Table 1. Fig. 19 exhibits an area of sample 13-4 riddled with holes and depressions between grains. Fig. 20, 20a - 20f shows metal cation concentration or loss in this area.

In sample 14-4 grain boundaries and grain forms are evident; see Fig. 21. However, there are not as many pores or holes showing. Black spot regions, though, are prevalent on the grain surfaces. Fig. 22 shows these areas rather vividly; SEM/EDX analysis indicates them to be areas of low chromium, low nickel and high iron concentration associated with potassium and sulfur. These areas are probably the beginning of reaction sites on the stainless steel surface. Fig. 23 is a high magnification micrograph of one such spot. EDX analysis, Fig. 23a and 23b, indicates low chromium and low nickel along with potassium and sulfur in that spot with high metal cation concentration surrounding blackish area.

A random sample of 304 stainless steel was selected for SEM/EDX analysis and used as a comparison to the specimens placed in the corrosive environment. Prior to sectioning, the sample was cleaned with 10% HNO_3

at 50°C for 20 minute cycles in an ultrasonic bath. A comparison of this surface to the surfaces exposed to the corrosive environment shows that, while grain boundaries are evident in both cases, figures 24-26, intergranular and surface attack seems to be occurring in the latter cases. EDX examination of the surface of the unexposed specimen revealed no non-uniform distribution of nickel, chromium or iron.

Plans: Specimens of Type 316 stainless steel will be evaluated under oxygen rich conditions with a mixture of 80% by weight K_2CO_3 and 20% by weight K_2SO_4. These specimens will be analyzed by SEM/EDX techniques. Further gravimetric and SEM/EDX analysis will be conducted on Type 304 stainless steels.

Table 1. Wastage

Specimen No.	Specimen Stainless Steel Type	Seed	Gas Stream State	Specimen Temperature °C	Weight In Grams Before Test	Weight In Grams After Test and Cleaning	Change In Weight In Grams*
4-6	316	K_2SO_4	O_2 Rich	590	72.427	72.417	-0.010
13-4	304	K_2SO_4	O_2 Rich	590	69.257	69.071	-0.186
14-4	304	K_2SO_4	O_2 Rich	400	65.853	65.850	-0.003

*It should be noted that of the total length of the specimen, around 250 mm, only a 75 mm section, in the middle, is subjected to the seeded gas stream.

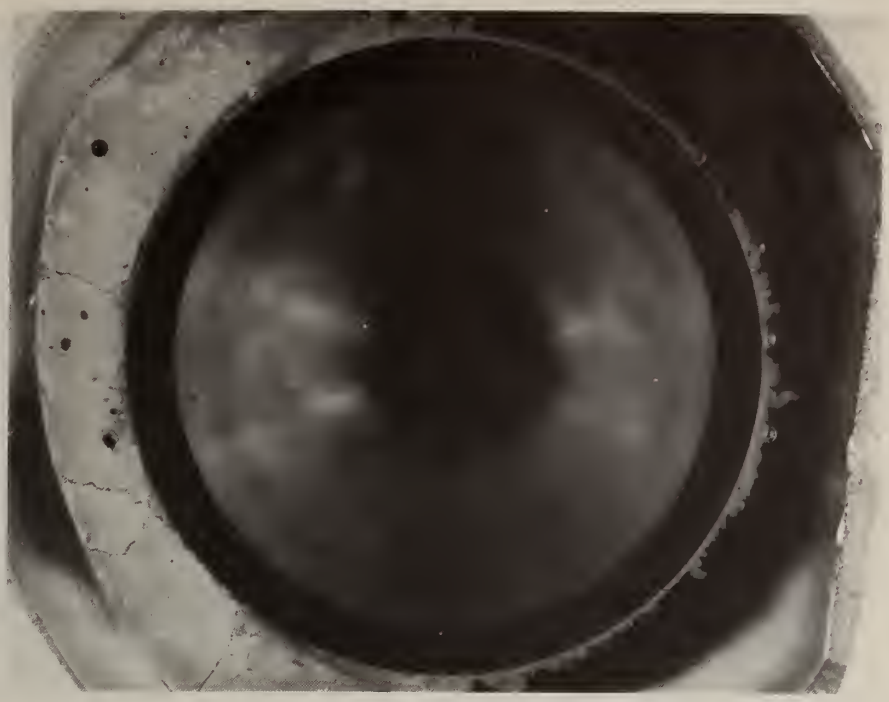

Fig. 1. Section of Type 316 stainless steel tubing after exposure to K_2SO_4 seeded oxygen rich hot gas stream. Note formation of deposit on the upper surface. Tube temperature 590 °C.

Fig. 2. Section of Type 316 stainless steel tubing after exposure to K_2SO_4 seeded oxygen rich hot gas stream. Note formation of deposit on the upper surface. Tube temperature 500 °C.

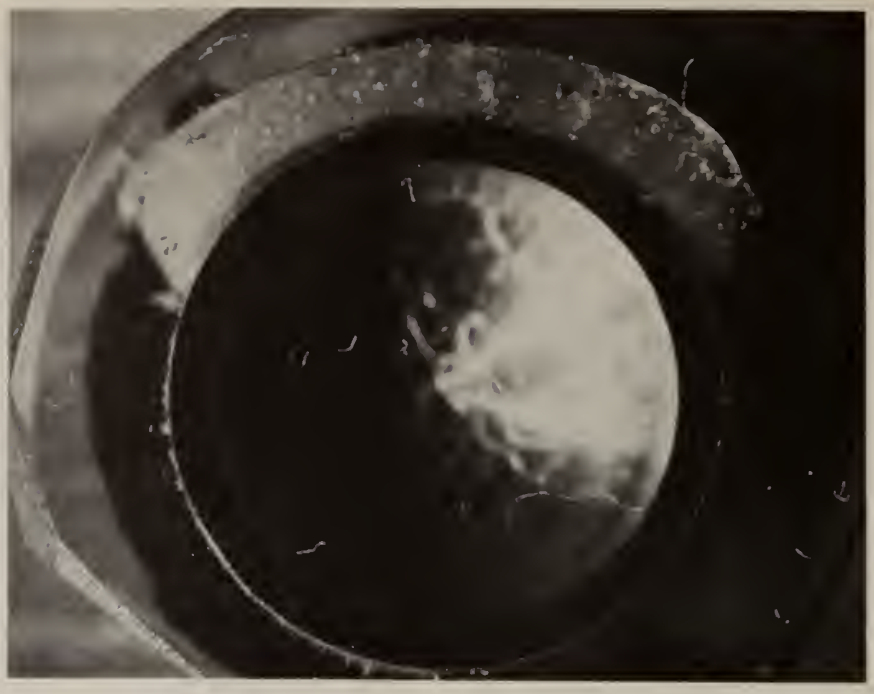

Fig. 3. Section of Type 316 stainless steel tubing after exposure to K_2SO_4 seeded oxygen rich hot gas stream. Note formation of coating on the upper surface. Tube temperature 400 °C.

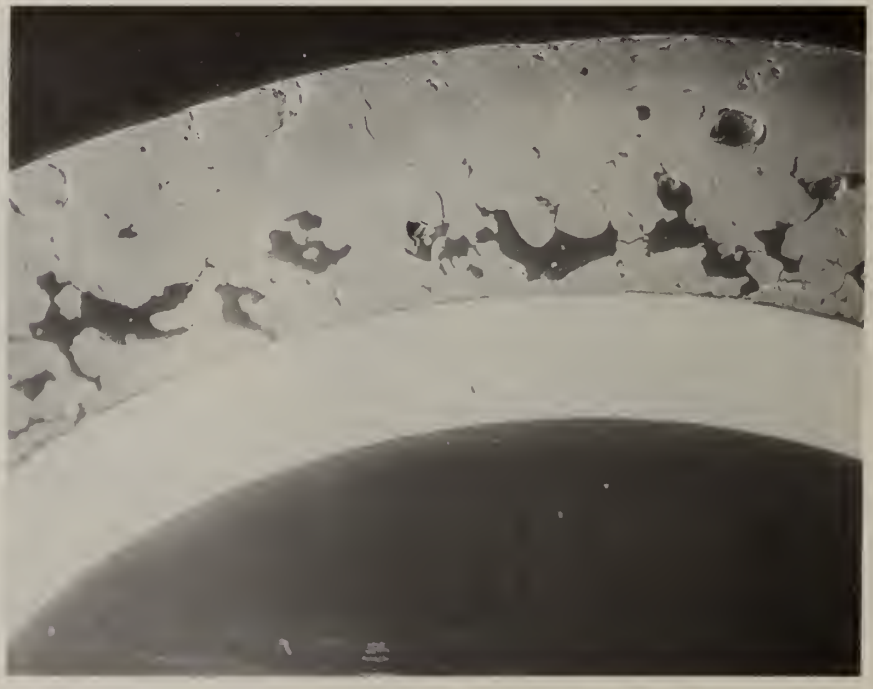

Fig. 4. SEM micrograph, 20 X, of K_2SO_4 deposit on leading surface of Type 316 stainless steel. Specimen temperature 590 °C, gas stream oxygen rich.

Fig. 5. SEM micrograph, 200 X, of gas stream-depost interface showing potassium rich band.

Fig. 6. SEM micrograph, 500 X of Type 316 stainless steel-deposit interface. Specimen temperature 590 °C, gas stream, oxygen rich.

Fig. 7. SEM micrograph, 2000 X, of center region of Fig. 6 showing reaction area at interface. Lettered regions correspond to labeled EDX spectra, Figs. 7a-7h. Specimen temperature 590 °C, gas stream oxygen rich.

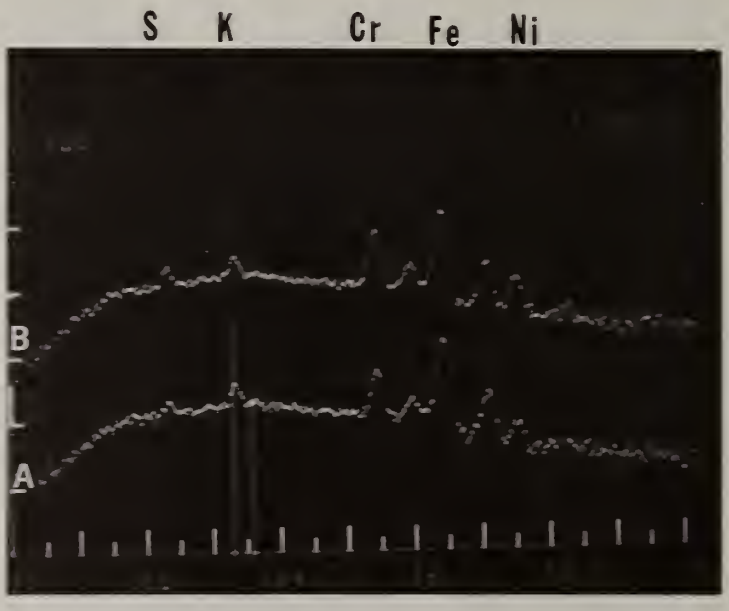

Fig. 7a. EDX spectra of regions A and B of Fig. 7 showing low Ni concentration areas. Specie positions and designations on all spectra in this section of this report are as indicated above.

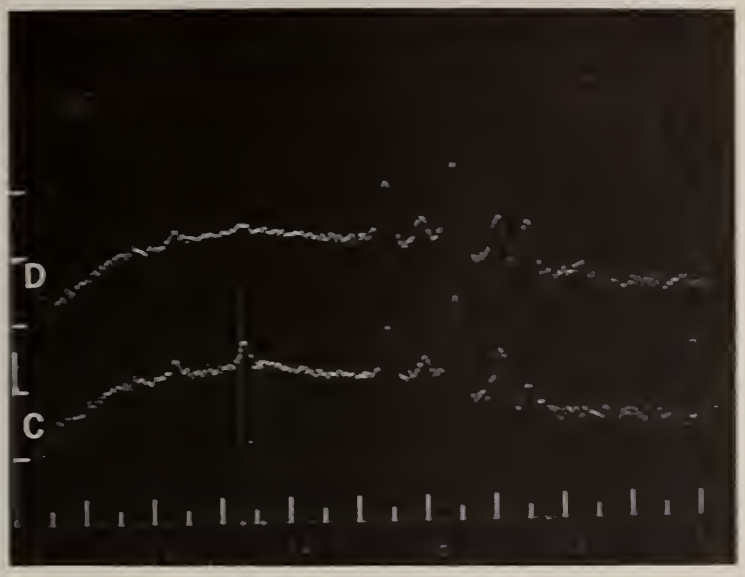

Fig. 7b. EDX spectra of regions C and D of Fig. 7 showing low Cr and low Ni concentrations in the reaction zone.

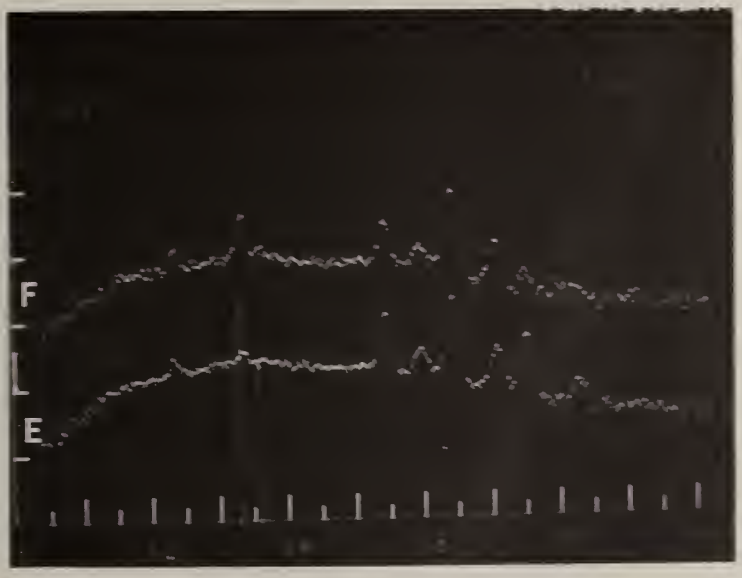

Fig. 7c. EDX spectra of regions E and F of Fig. 7 showing high Ni and low Cr concentrations.

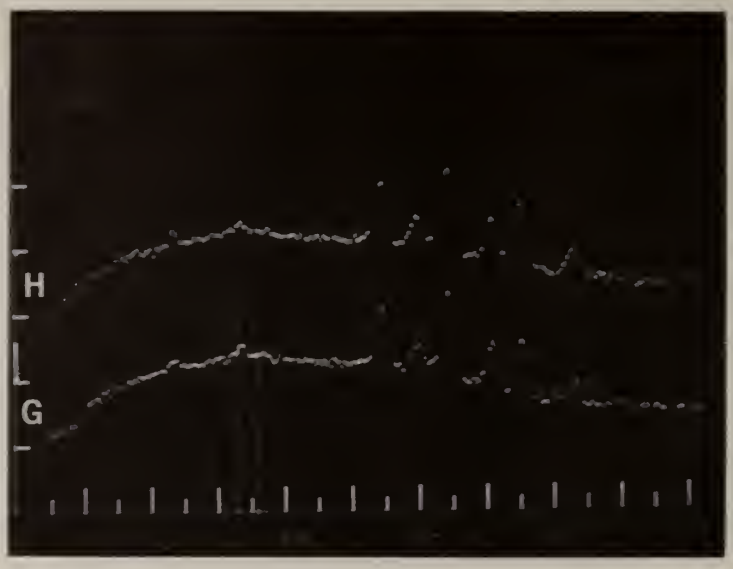

Fig. 7d. EDX spectra of regions G and H of Fig. 7 showing high Ni at the metal edge.

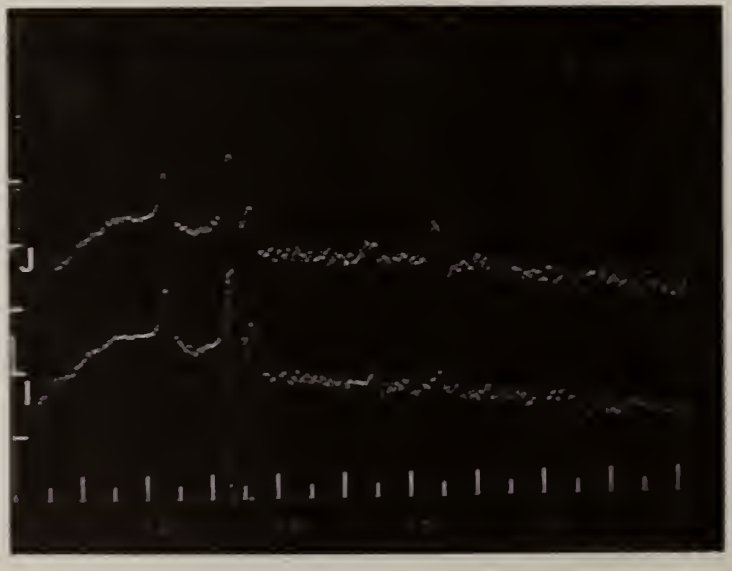

Fig. 7e. EDX spectra of regions I and J of Fig. 7 showing Fe penetration into the deposit.

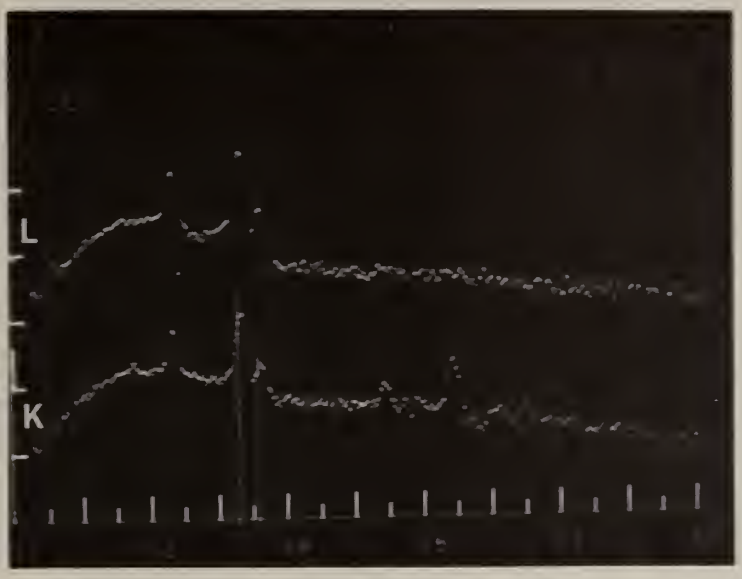

Fig. 7f. EDX spectra of regions K and L of Fig. 7 showing Fe and Cr penetration into the deposit.

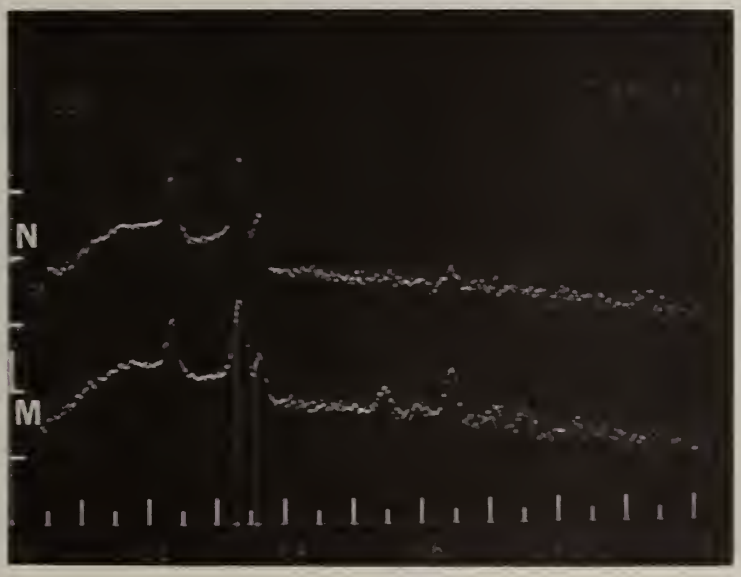

Fig. 7g. EDX spectra of regions M and N of Fig. 7 showing again Fe and Cr penetration into the potassium-sulfur deposit.

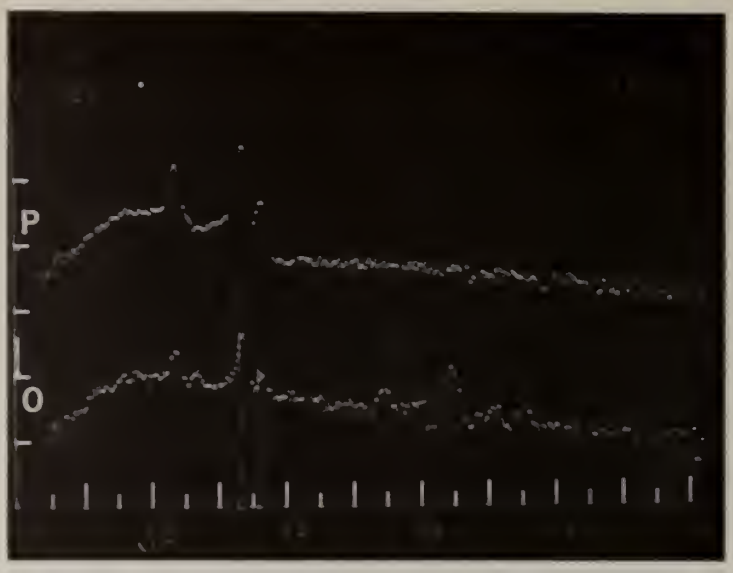

Fig. 7h. EDX spectra of regions O and P of Fig. 7 showing penetration of all three species, Fe and Cr and Ni into the deposit.

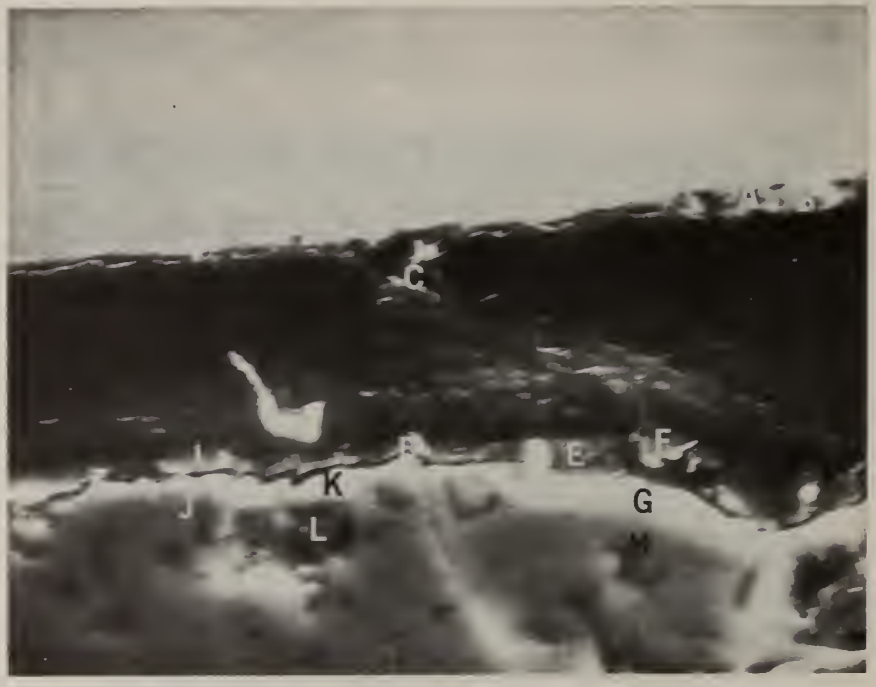

Fig. 8. SEM micrograph, 2000 X, of Type 316 stainless steel-deposit interface. Lettered regions correspond to labeled EDX spectra, Figs. 8a-8e. Specimen temperature 590 °C, gas stream oxygen rich.

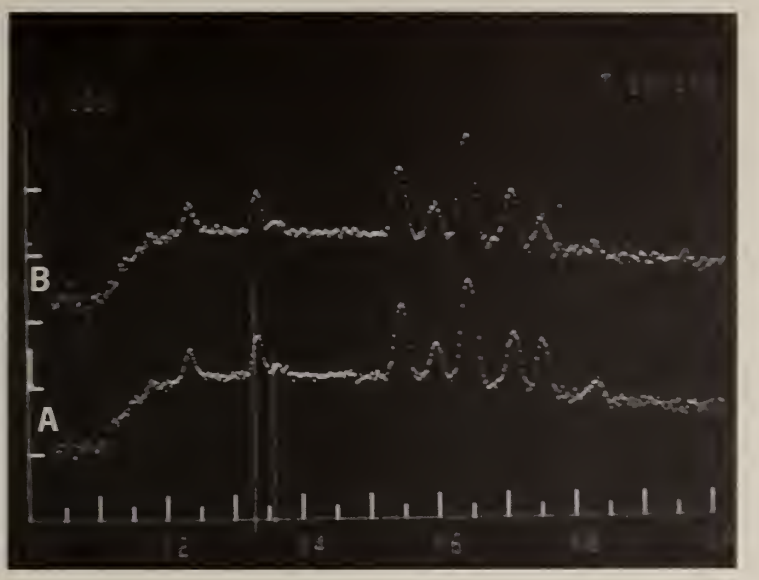

Fig. 8a. EDX spectra of regions A and B of Fig. 8 showing low Ni and low Cr concentrationsat the metal edge.

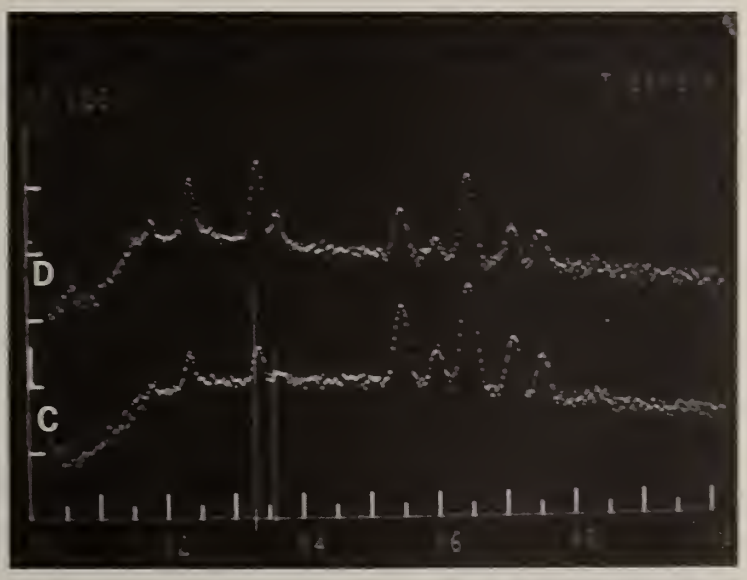

Fig. 8b. EDX spectra of regions C and D of Fig. 8 showing low Ni and low Cr concentrations at the metal edge.

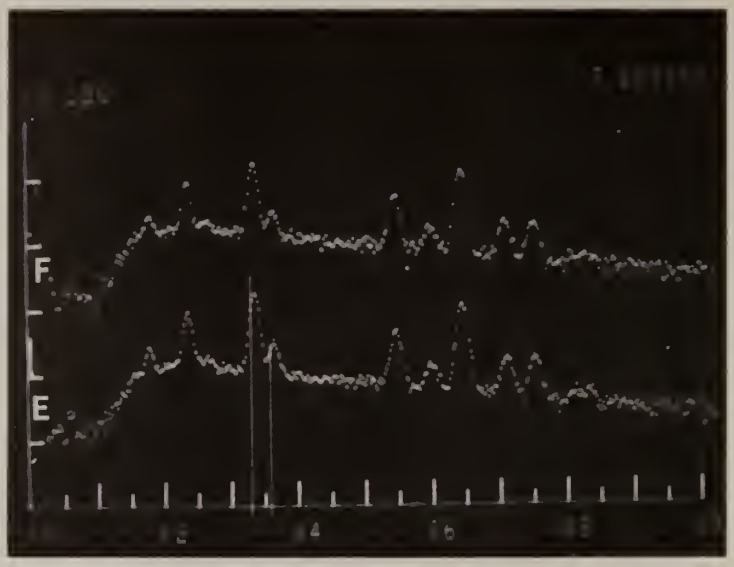

Fig. 8c. EDX spectra of regions E and F of Fig. 8 showing metal cations in the reaction zone of the deposit.

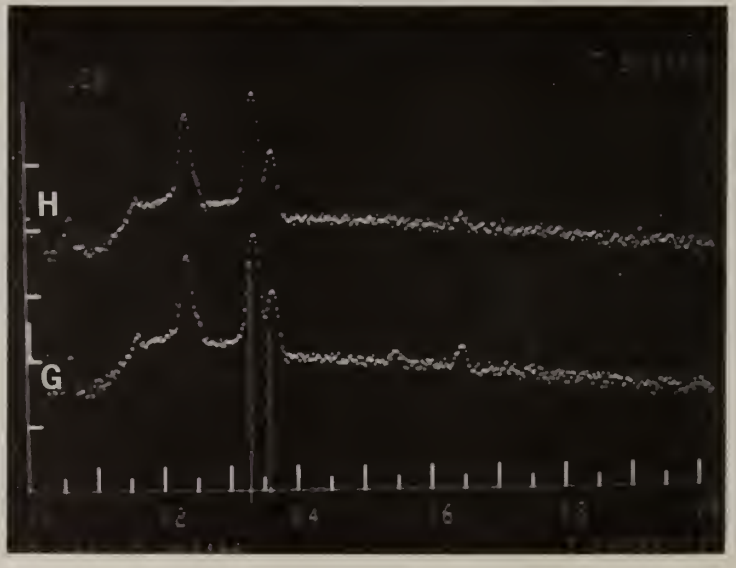

Fig. 8d. EDX spectra of regions G and H of Fig. 8 showing metal cations in the reaction zone of the deposit.

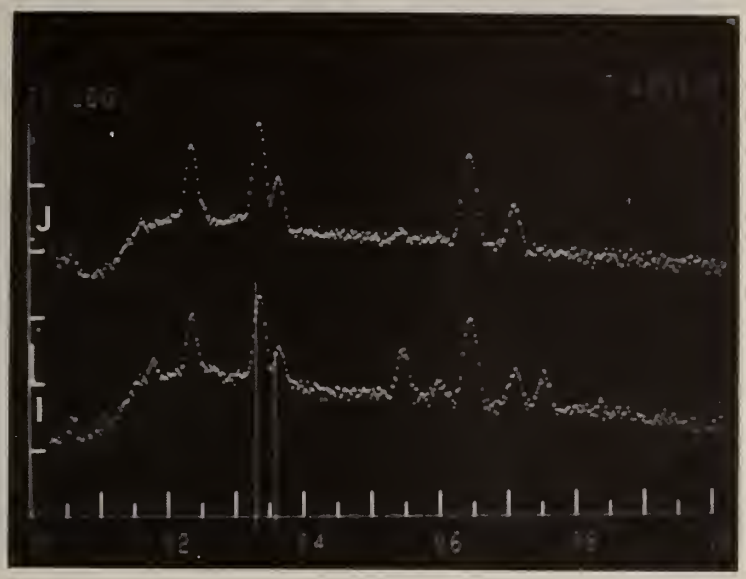

Fig. 8e. EDX spectra of regions I and J of Fig. 8 showing metal cations in the reaction zone of the deposit.

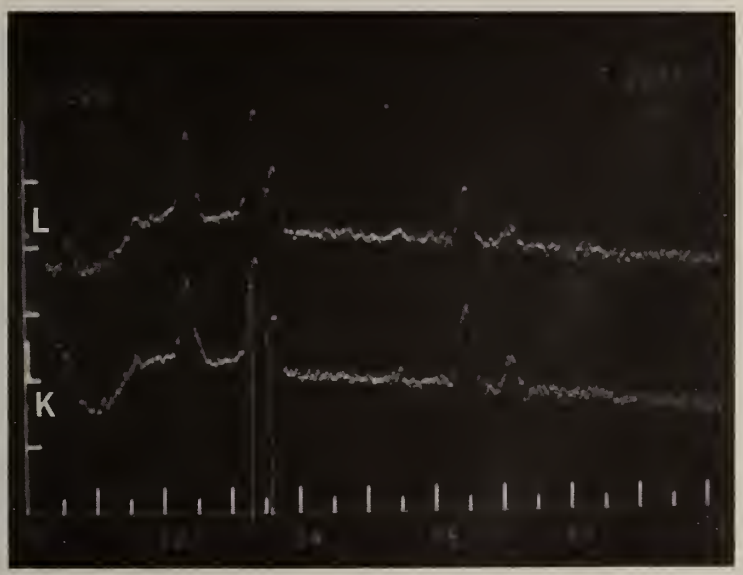

Fig. 9. EDX spectra of regions K and L of Fig. 8 showing Fe farther back in the deposit.

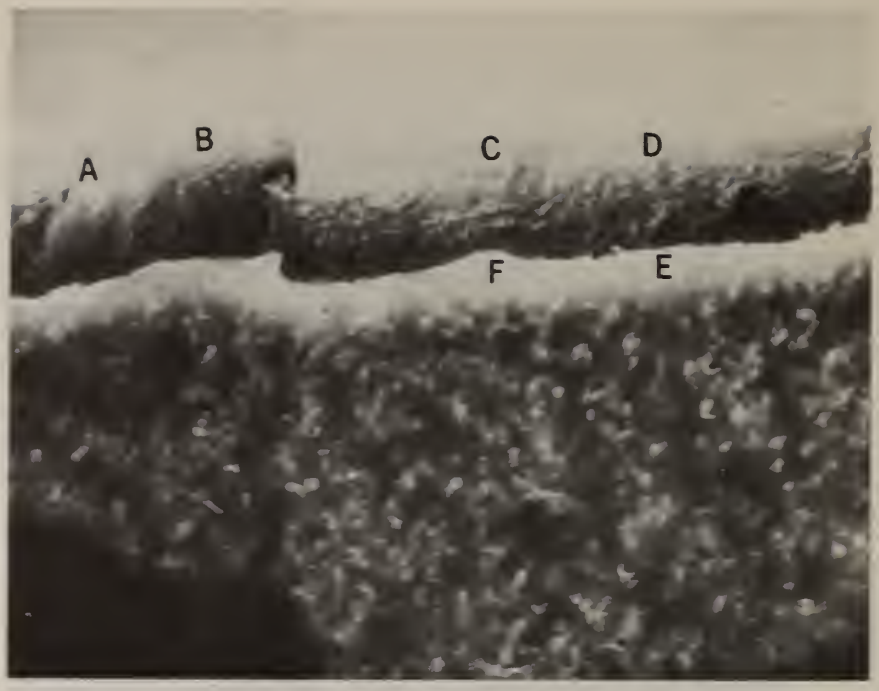

Fig. 10. SEM micrograph, 2000 X, of Type 316 stainless steel-fume deposit interface. Lettered regions correspond to labeled EDX spectra Figs. 10a-10c.

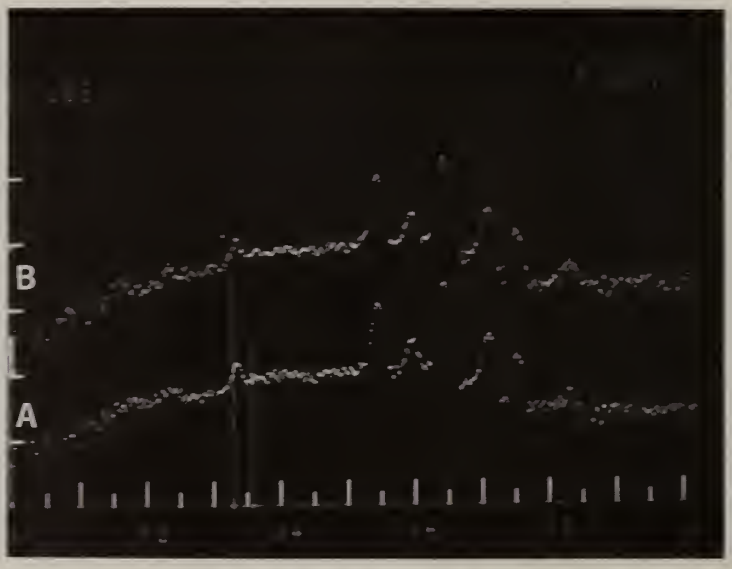

Fig. 10a. EDX spectra of regions A and B of Fig. 10 showing distribution of Cr, Fe and Ni at the stainless steel edge.

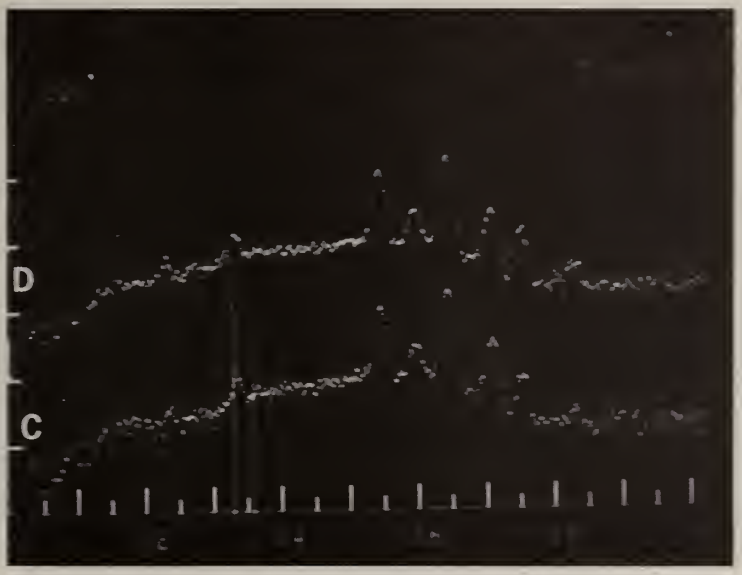

Fig. 10b. EDX spectra of regions C and D of Fig. 10 showing distribution of Cr, Fe and Ni at the stainless steel edge.

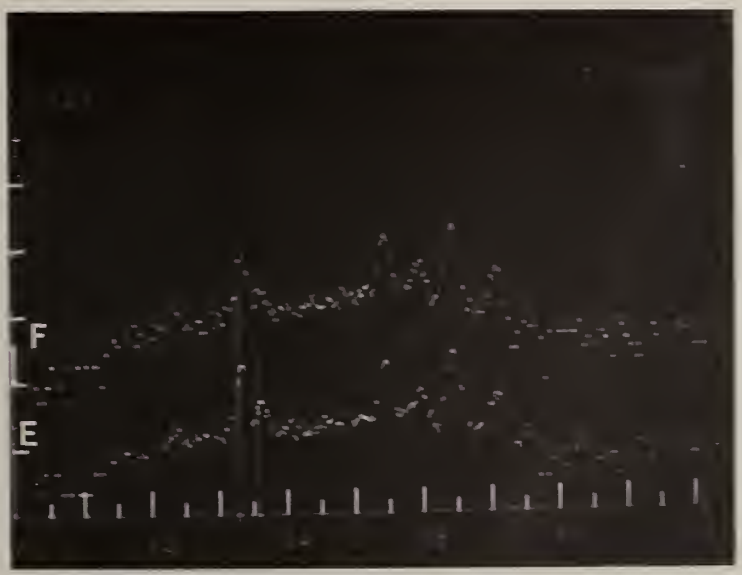

Fig. 10c. EDX spectra of regions E and F of Fig. 10 showing absence of Ni in the reaction zone.

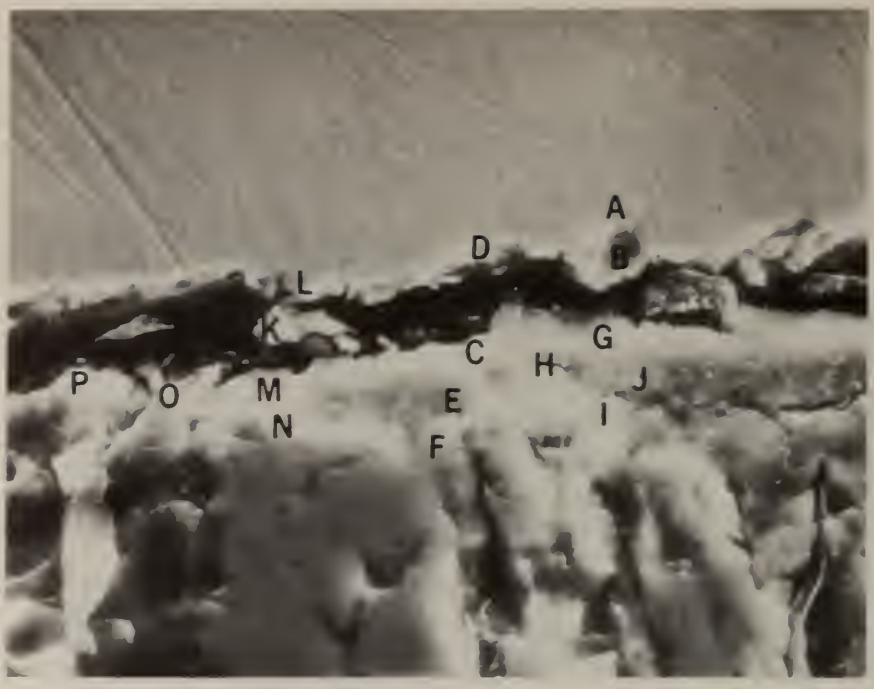

Fig. 11. SEM micrograph, 2000 X of Type 316 stainless steel-deposit interface. Lettered regions correspond to labeled EDX spectra Figs. 11a-11h. Specimen temperature 500 °C, gas stream oxygen rich.

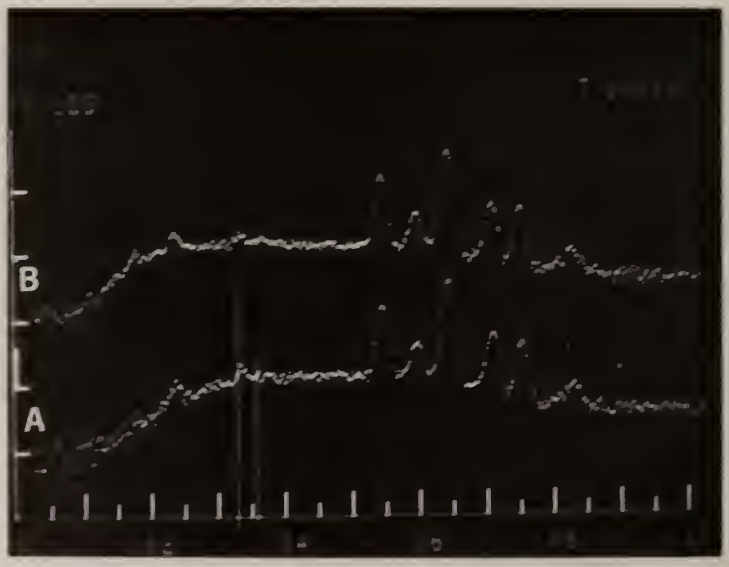

Fig. 11a. EDX spectra of regions A and B of Fig. 11 showing slight loss of Ni at stainless steel edge as compared to the bulk.

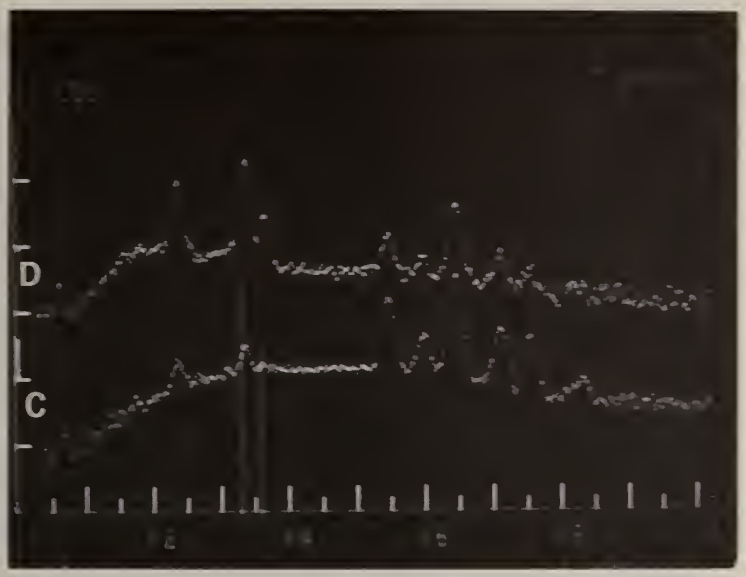

Fig. 11b. EDX spectra of regions C and D of Fig. 11 showing high Fe and low Cr and Ni concentrations in reaction zone.

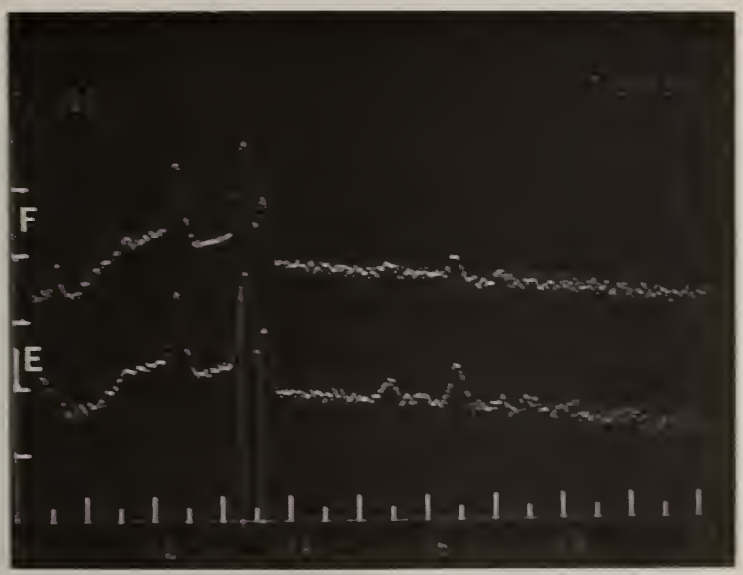

Fig. 11c. EDX spectra of regions E and F of Fig. 11 showing the penetration of Fe in the deposit.

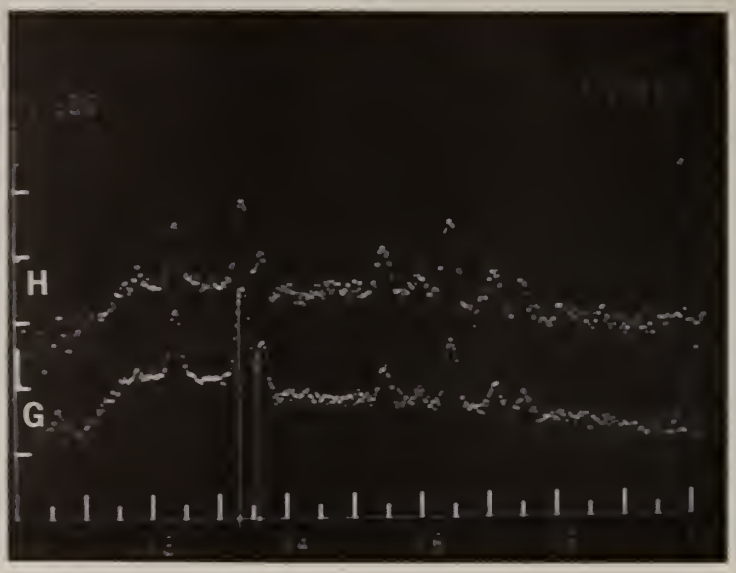

Fig. 11d. EDX spectra of regions G and H of Fig. 11 showing concentrations of Fe, Cr and Ni in the reaction zone of the stainless steel-deposit interface.

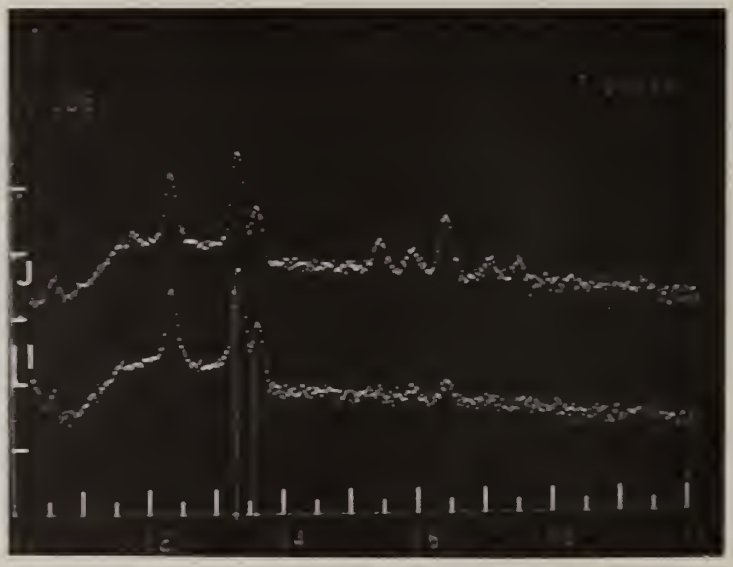

Fig. 11e. EDX spectra of regions I and J of Fig. 11 showing penetration of Fe, Cr and Ni in the deposit.

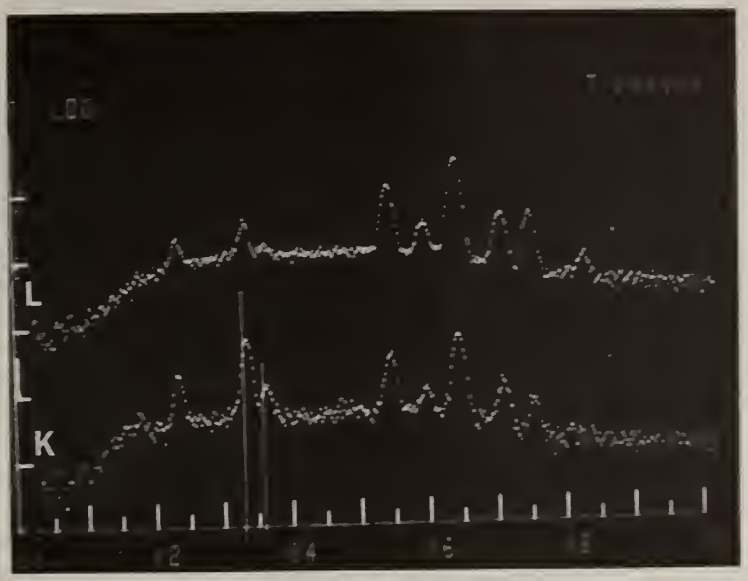

Fig. 11f. EDX spectra of regions K and L of Fig. 11 showing concentration of Fe, Cr and Ni at the metal edge.

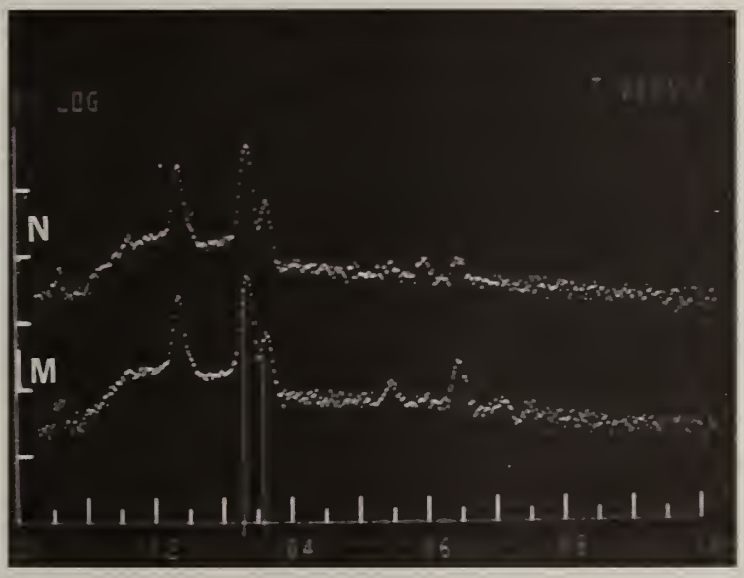

Fig. 11g. EDX spectra of regions M and N of Fig. 11 showing low concentration of Fe in reaction zone.

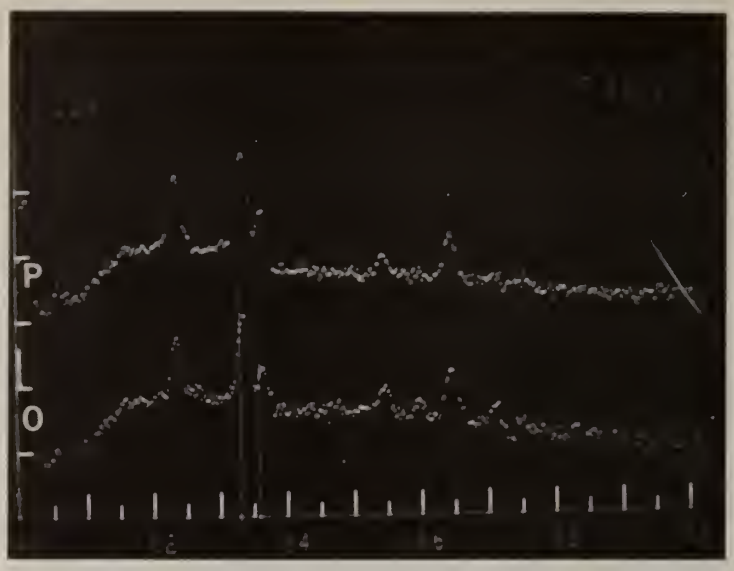

Fig. 11h. EDX spectra of regions O and P of Fig. 11 showing concentrations of Fe, Cr and Ni in the reaction zone.

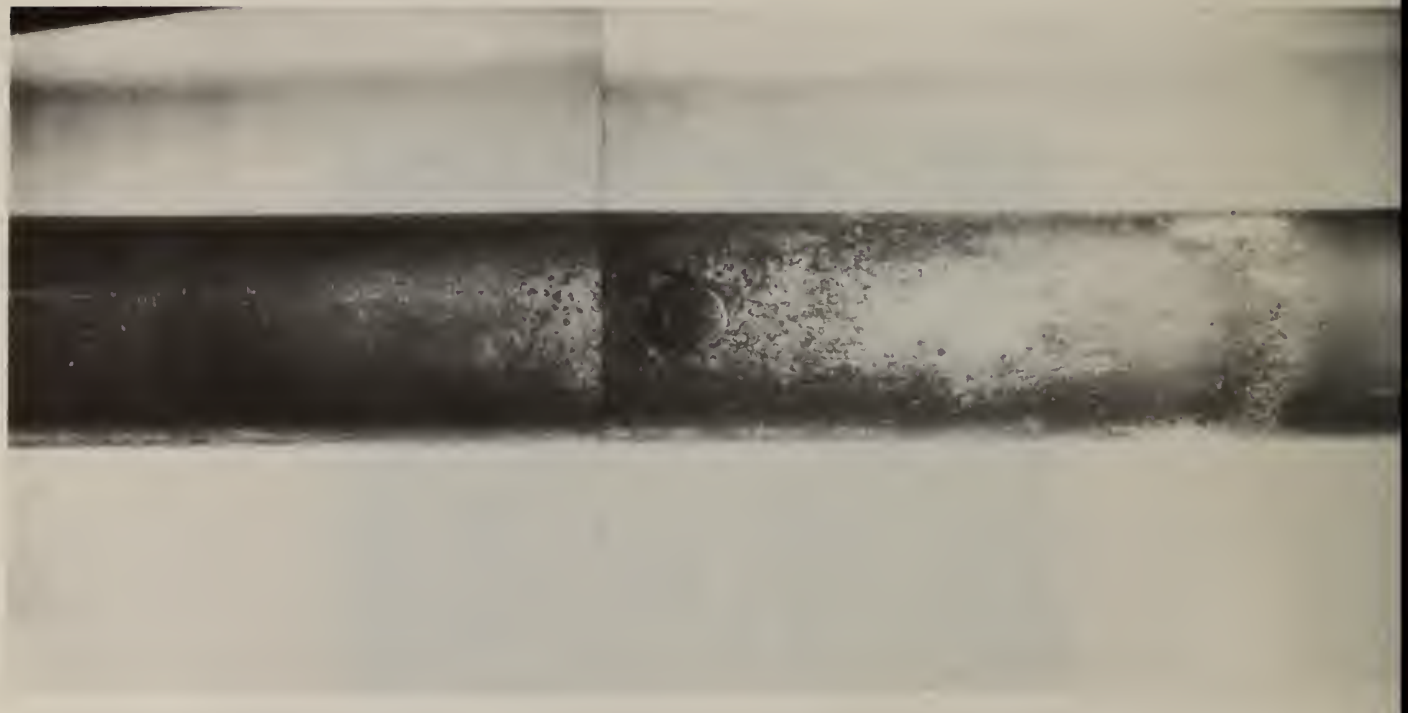

Fig. 12. Type 316 stainless steel after exposure for 4 hours at 590 °C to K_2SO_4 seeded, oxygen rich hot gas stream and subsequent cleaning. Approximately 2 X.

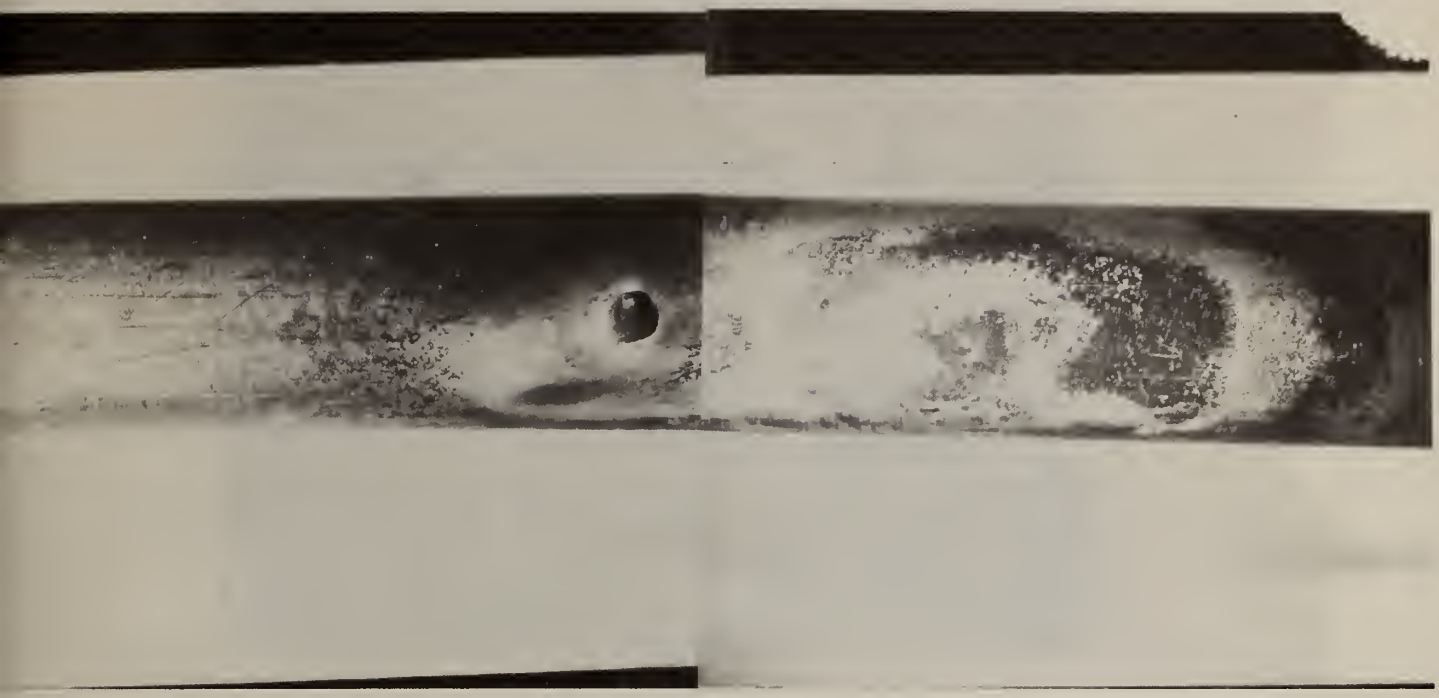

Fig. 13. Type 304 stainless steel after exposure for 4 hours at 590 °C to K_2SO_4 seeded, oxygen rich hot gas stream and subsequent cleaning. Approximately 2 X.

Fig. 14. Type 304 stainless steel after exposure for 4 hours at 400 °C to K_2SO_4 seeded, oxygen rich hot gas stream and subsequent cleaning. Approximately 2 X.

Fig. 15. SEM micrograph, 400 X, of Type 316 stainless steel exposed for 4 hours at 590 °C to K_2SO_4 seeded, oxygen rich hot gas stream.

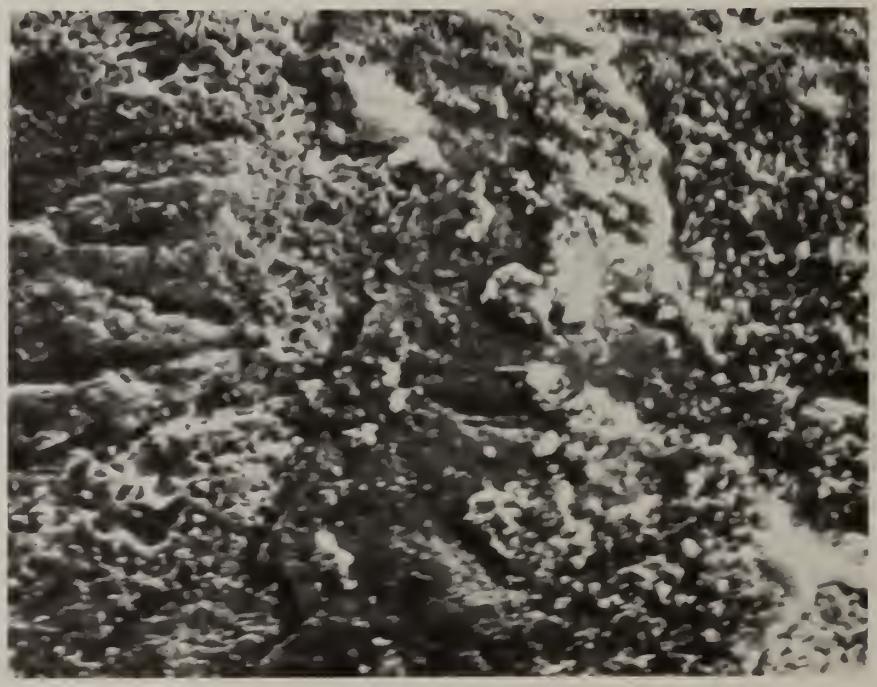

Fig. 16. SEM micrograph, 1600 X, of mid region of Fig. 15 showing surface attack.

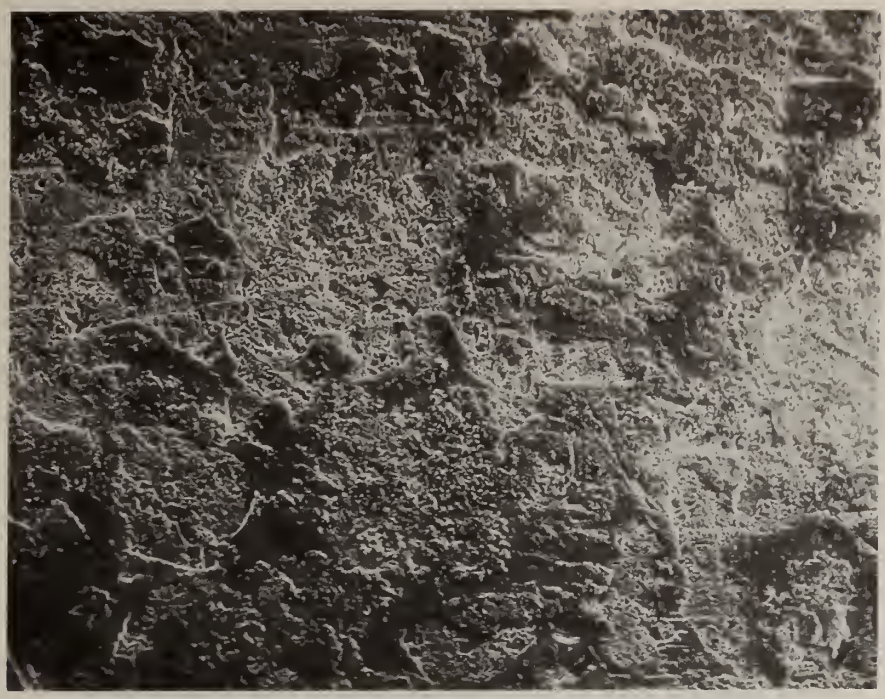

Fig. 17. SEM micrograph, 400 X, of Type 316 stainless steel exposed for 4 hours at 590 °C to K_2SO_4 seeded, oxygen rich hot gas stream.

Fig. 18. SEM micrograph, 1600 X, of mid region of Fig. 17 showing surface attack. Labeled regions correspond to labeled EDX spectra, Figs. 18a-18c.

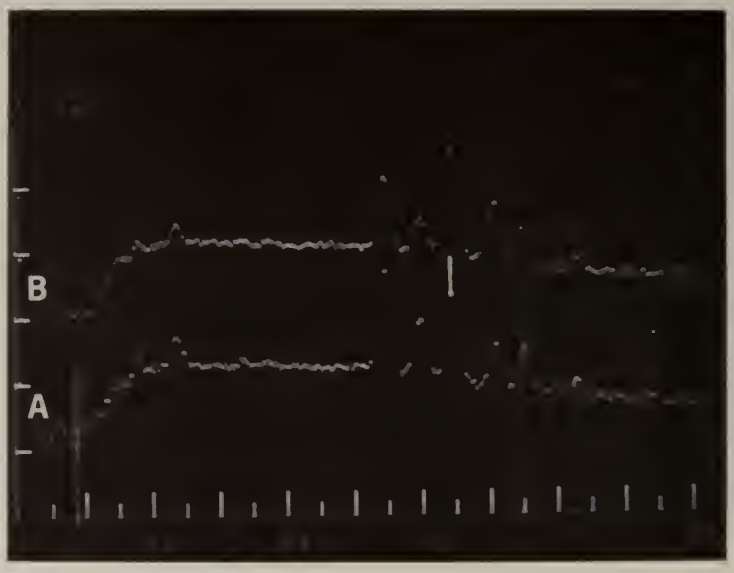

Fig. 18a. EDX spectra of regions A and B of Fig. 18 showing low Ni and high Cr concentrations.

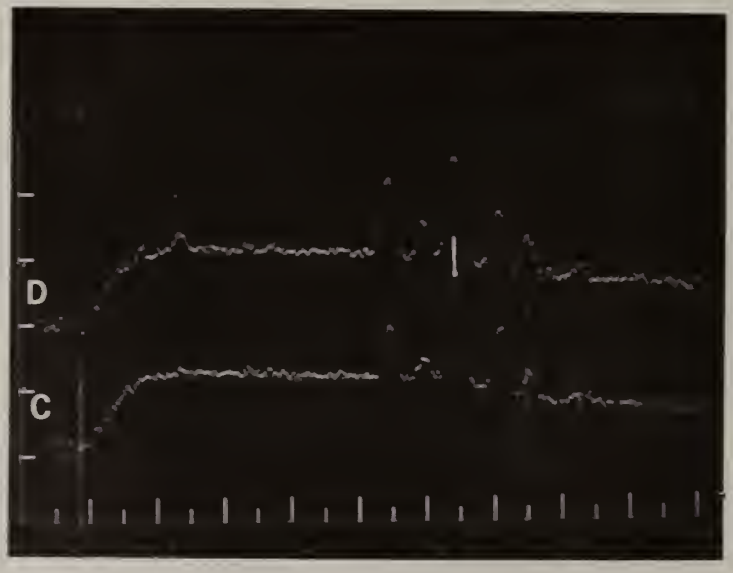

Fig. 18b. EDX spectra of regions C and D of Fig. 18 showing high Ni and high Cr concentrations.

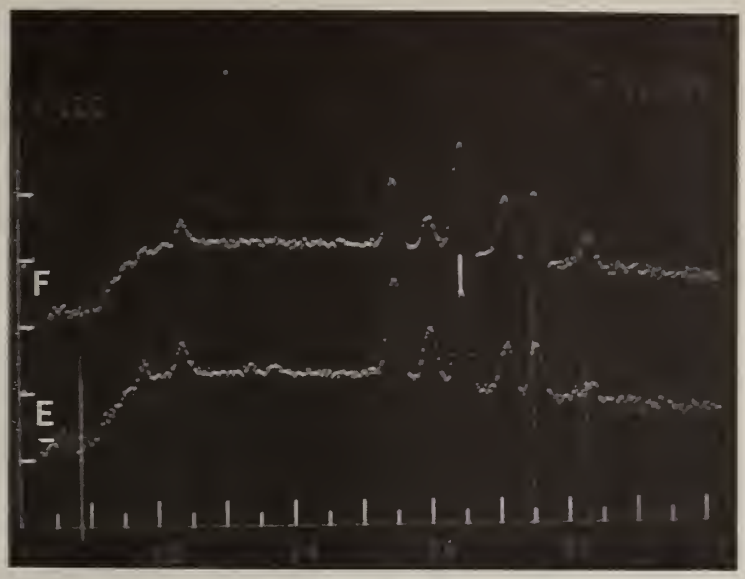

Fig. 18c. EDX spectra of regions E and F of Fig. 13 showing low Ni and high Fe concentrations.

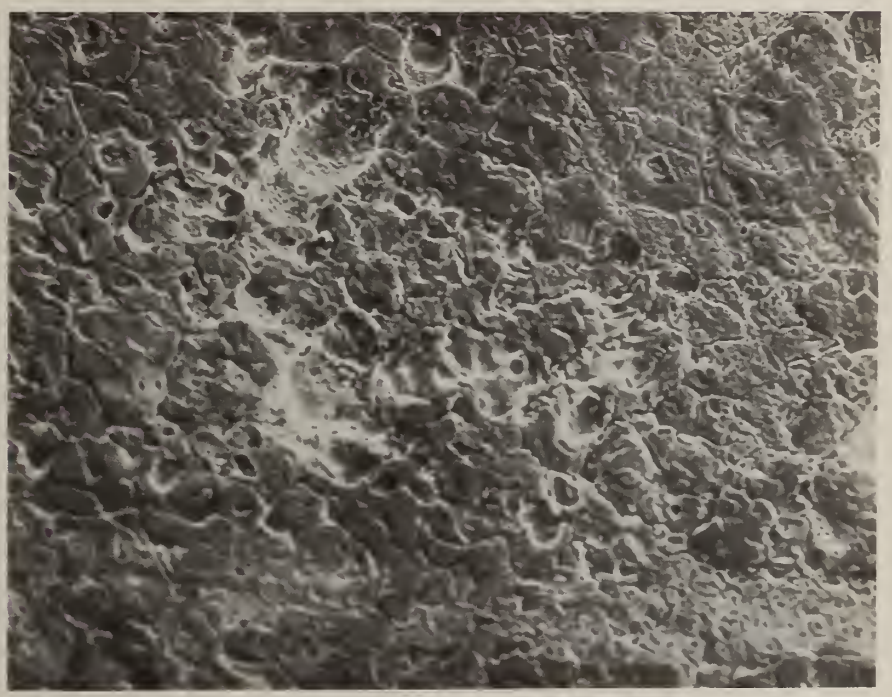

Fig. 19. SEM micrograph, 450 X, of Type 304 stainless steel exposed for 4 hours at 590 °C to a K_2SO_4 seeded, oxygen rich hot gas stream.

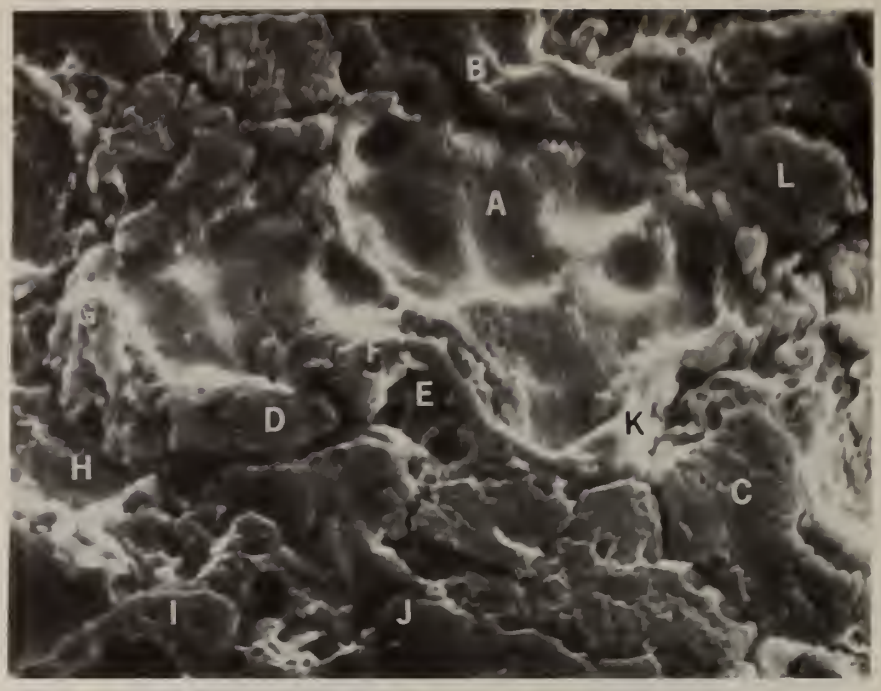

Fig. 20. SEM micrograph, 1900 X, of the mid region of Fig. 19 showing surface attack. Labeled regions correspond to labeled EDX spectra, Figs. 20a-20f.

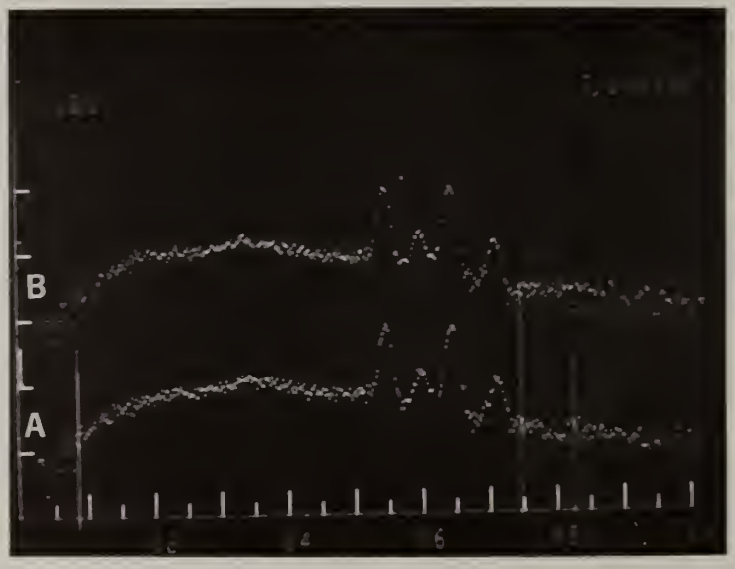

Fig. 20a. EDX spectra of regions A and B of Fig. 20 showing Ni depleted regions.

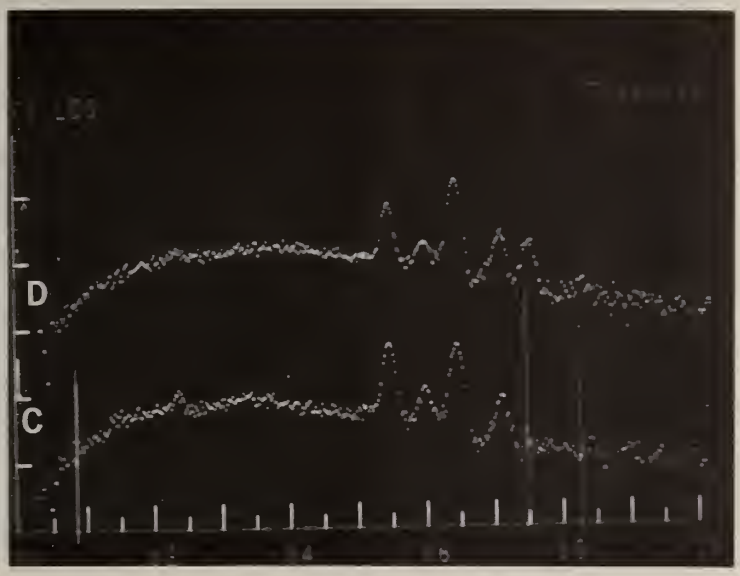

Fig. 20b. EDX spectra of regions C and D of Fig. 20 showing another Ni depleted region.

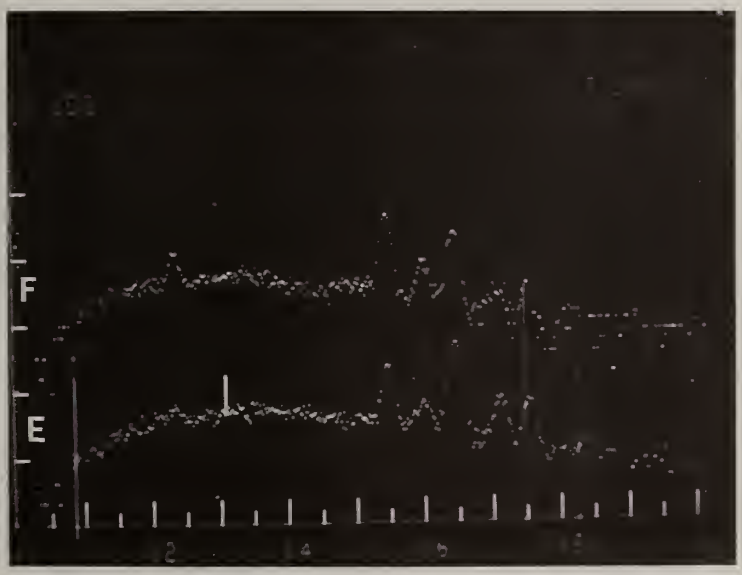

Fig. 20c. EDX spectra of regions E and F of Fig. 20 showing a region of high Cr concentration.

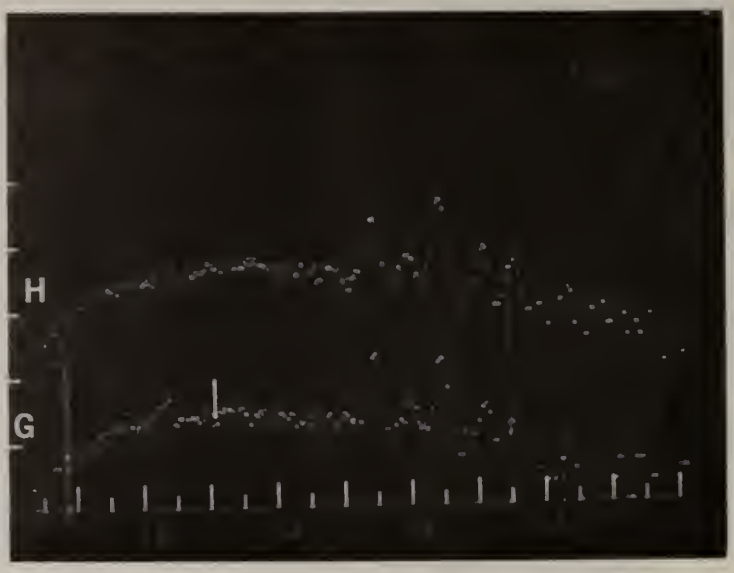

Fig. 20d. EDX spectra of regions G and H of Fig. 20 showing another region of high Cr concentration.

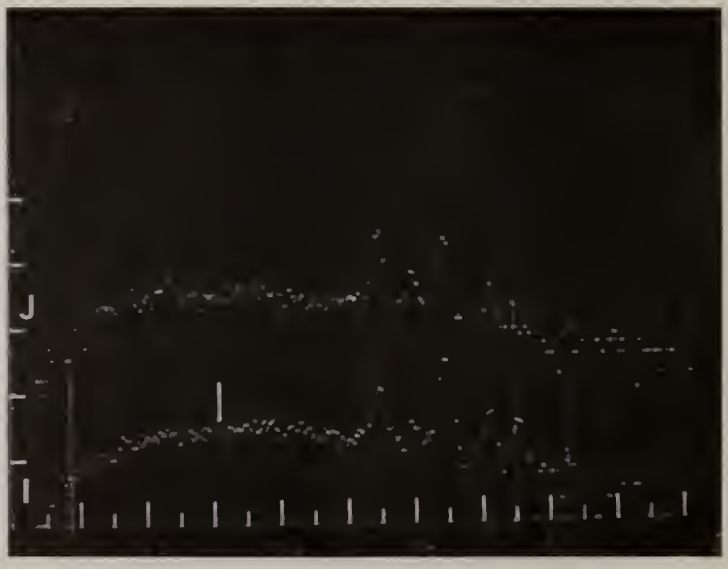

Fig. 20e. EDX spectra of regions I and J of Fig. 20 showing another region of high Cr concentration.

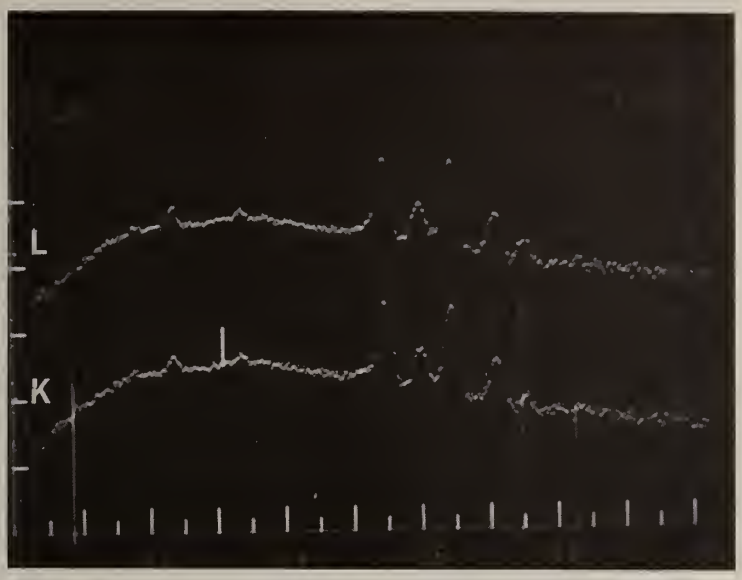

Fig. 20f. EDX spectra of regions K and L of Fig. 20 showing regions of high Cr and low Ni concentrations.

Fig. 21. SEM micrograph, 350 X, of Type 304 stainless steel specimen 14-4, exposed for 4 hours to a K_2SO_4 seeded oxygen rich hot gas stream.

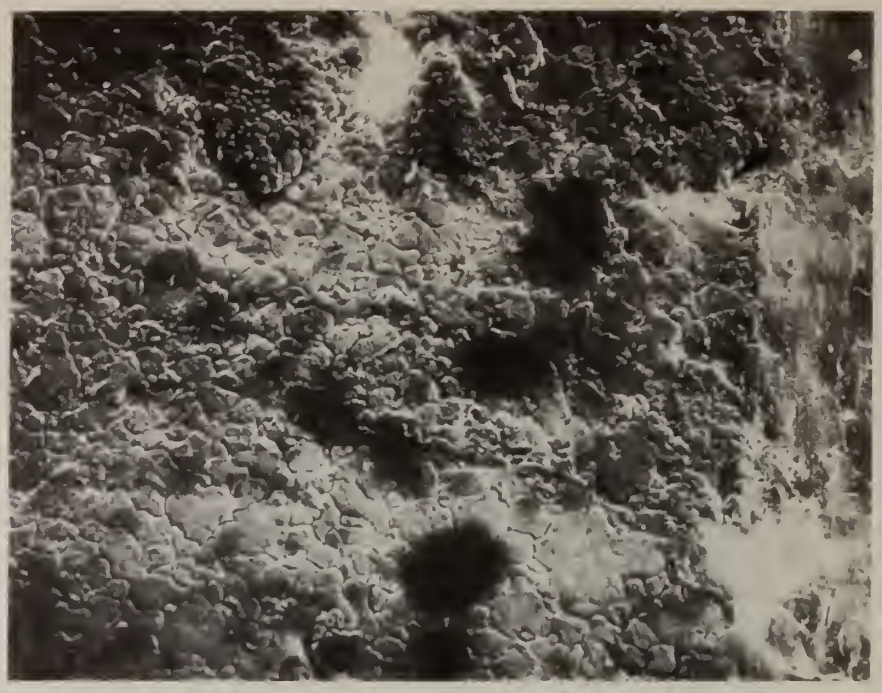

Fig. 22. SEM micrograph, 375 X, of another region specimen 14-4 showing what appears to be the onset of corrosion.

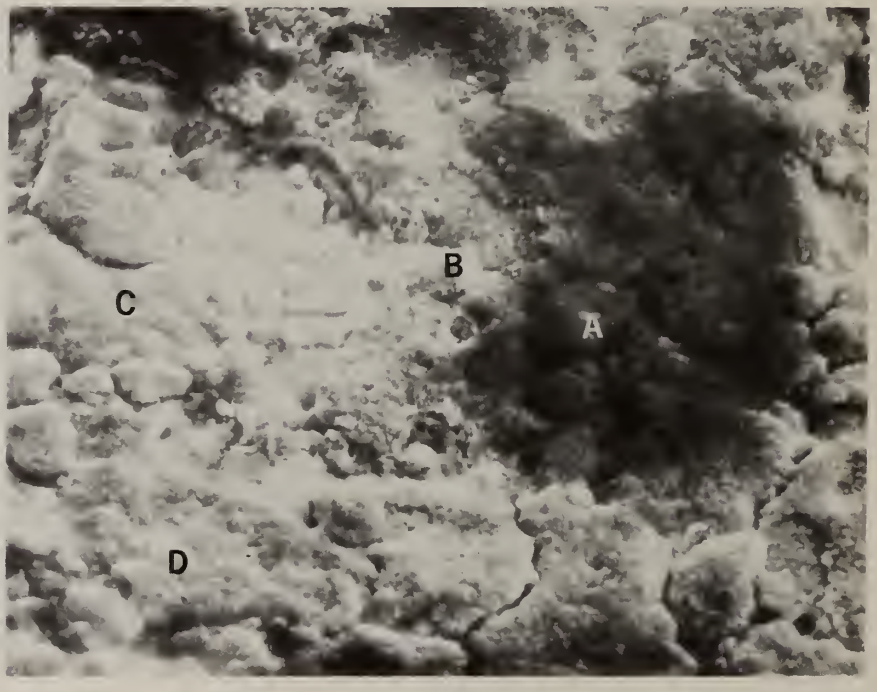

Fig. 23. SEM micrograph, 1500 X, of the mid region of Fig. 22. Labeled regions correspond to labeled EDX spectra, Figs. 23a and 23b.

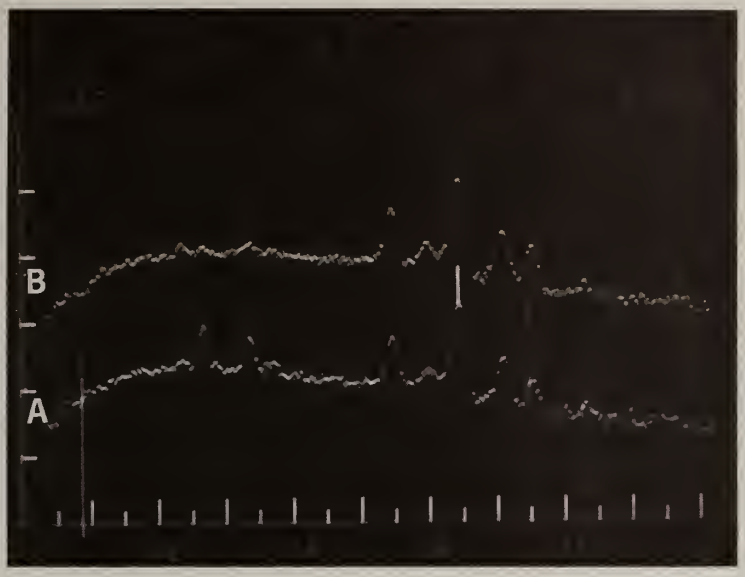

Fig. 23a. EDX spectra of regions A and B of Fig. 23 showing nickel depletion in a dark region.

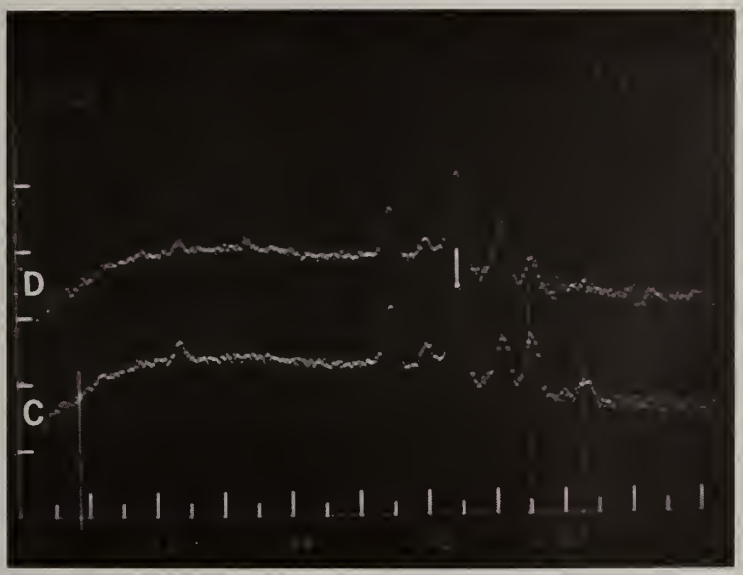

Fig. 23b. EDX spectra of regions C and D of Fig. 23 showing a Ni depleted region C and a region of high Ni and high Cr concentration.

Fig. 24. SEM micrograph of Type 304 stainless steel, unexposed but cleaned. Note grains and grain boundaries, 1600 X.

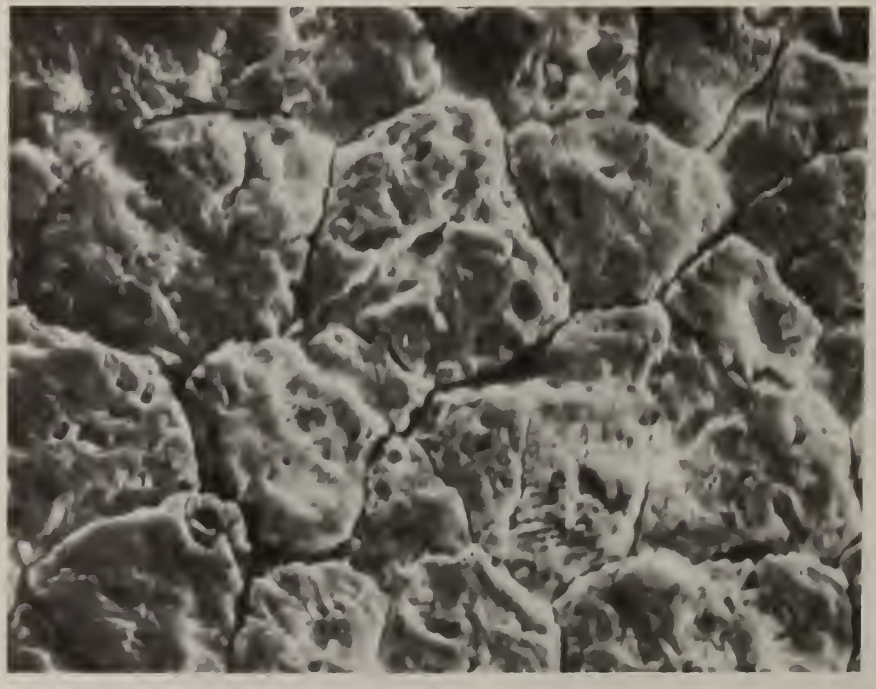

Fig. 25. SEM micrograph, 1900 X, of Type 304 stainless steel after exposure for 4 hours at 590 °C to a K_2SO_4 seeded hot gas stream and subsequent cleaning. Note grain boundaries and grain surface.

Fig. 26. SEM micrograph, 1400 X, of Type 304 stainless steel after exposure for 4 hours at 400 °C to a K_2SO_4 seeded hot gas stream and subsequent cleaning. Note grain boundaries and grain surface.